Supplementary information for
Optimised optical waveforms drive efficient water window attosecond pulse generation

Miguel A. Silva-Toledo[1,2,*], Fabian Scheiba[1,2,*], Maximilian Kubullek[1,2], Rafael de Q. Garcia[1,2], Roland E. Mainz[1,2], Giulio Maria Rossi[1,2,3], and Franz X. Kärtner[1,2]

[1]*Center for Free-Electron Laser Science CFEL, Deutsches Elektronen-Synchrotron DESY, Notkestr. 85, 22607 Hamburg, Germany*

[2]*Physics Department and The Hamburg Centre for Ultrafast Imaging, University of Hamburg, Luruper Chaussee 149, 22761 Hamburg, Germany*

[3]*email: giulio.maria.rossi@desy.de*

∗*These Authors contributed equally*

Contents

1 Experiment

1.1 Measurement procedure

This section describes the measurement procedures that were followed for the acquisition of the presented data. The experiment was carried out for Helium and Neon as the high-harmonic generation (HHG) target. Additionally, all HHG measurements were repeated for multiple different peak intensities of the driving waveforms using a set of neutral density filters; the used filters were: ND0.0 (uncoated substrate), ND0.1, ND0.2, and ND0.3. The slight thickness differences between the filters were characterised independently and are used to relate the different measurements. The driving waveform energies for the different filters are given in Table 1.

Table 1: **Measured NIR and IR pulse energies at the gas target for the different ND filters.** The ND 0.0 filter corresponds to the 2-mm UV fused silica substrate without the reflective coating.

ND	NIR (μJ)	IR (μJ)	Total (μJ)
0.0	20	170	190
0.1	19	163	182
0.2	16	126	142
0.3	11	77	88

A complete dataset for one combination of gas-type and neutral density filter is produced using the following steps:

1. **Determination of best IR-only phase-matching parameters:** HHG spectra are recorded

while scanning the position of the gas-cell relative to the focus for a set of different backing pressures. The measurements are carried out using only the IR-pulse while averaging over its CEP. From this set of measurements the combination (P_b,z_{PM}) maximising the IR-only yield is determined. The found combination was kept fixed for all following measurements.

2. **IR CEP scan:** HHG spectra are recorded at the found (P_b,z_{PM}) combination while scanning the CEP of the IR-pulse. The scan is used to determine the highest possible yield for the IR field case for specific HHG photon energy ranges.

3. **In-situ waveform characterization:** A TREX measurement (see Section 1.3) is carried out at the optimised target position (z_{PM}), using helium at a backing pressure of 1 bar and the strongest attenuating neutral density filter ND0.3 to avoid ionisation, which would prohibit a proper reconstruction of the pulses. In addition to knowledge of all used driving waveforms in the subsequent measurements, the reconstruction also gives the precise time-zero between the IR- and NIR-pulse for the relative delay scans.

4. **Relative delay scans at different CEPs:** HHG spectra are recorded at the optimal (P_b, z_{PM}) combination determined in step 1 while scanning the relative delay between the constituent pulses around the established time-zero. Each scan is repeated for different CEP values: the reference CEP (the initial lock point) ϕ_0, $\phi_0 - \pi$/4, $\phi_0 - \pi$/2, and $\phi_0 - \pi$.

It is important to note that the phase lock between the constituent pulses was not broken from the TREX measurement onwards. This allows us to assign a driving waveform to each recorded HHG spectrum. We furthermore calibrate the spectra using additional measurements

with a calibrated XUV photodiode (see Section 1.7) allowing us to determine the absolute photon flux for each spectrum.

1.2 Determination of best IR field phase-matching parameters

Figure 1 shows HHG gas cell scans at different backing pressures and attenuations acquired using only the IR pulse, with Neon (2, 4, and 6 bar) and Helium (6, 8, and 10 bar). The (P_b,z_{PM}) combinations maximising the HHG-yield and cutoff for each attenuation are identified from these scans and listed in Table 2.

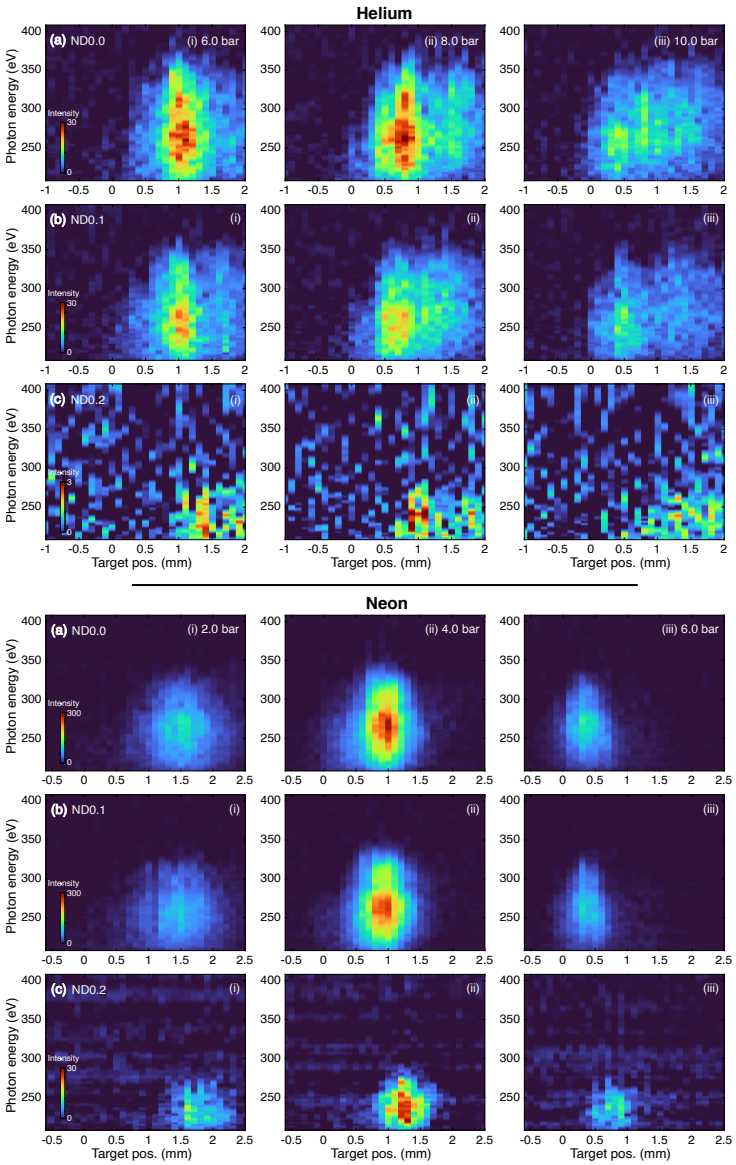

Figure 1: **HHG gas-cell scans in He and Ne driven by the IR pulse for different ND filters.** HHG spectra as a function of gas target position for ND filters: (a) 0.0, (b) 0.1, and (c) 0.2. Each panel shows scans in He (i: 6 bar, ii: 8 bar, iii: 10 bar) and Ne (i: 2 bar, ii: 4 bar, iii: 6 bar), with averaged CEP. The optical driving beam transmitted through the gas cell was blocked by a 150 nm Al filter. Each spectrum was integrated for 2 s.

Table 2: **Optimal macroscopic parameters for IR-only HHG.** Combinations of backing pressure P_b and gas target position z_{PM} for IR-only HHG in neon and helium, under various ND filters (see Figure 1).

ND	**Helium**		**Neon**	
	Backing pressure (bar)	Target pos. (mm)	Backing pressure (bar)	Target pos. (mm)
0.0	8.0	0.8	4.0	1.0
0.1	6.0	1.0	4.0	1.0
0.2	6.0	1.5	4.0	1.0

Figure 1 shows the influence, that the input pulse energy has on the cutofff energy and yield of HHG in Helium and Neon. Without additional attenuation (ND0.0), the cutoff reaches approximately 360 eV in Helium and 345 eV in Neon. When attenuating with ND0.1 the Helium cutoff decreases by around 15 eV while the Neon cutoff only drops by 5 eV. After further attenuation using ND0.2 the cutoff with both gases reduces significantly to only about 280 eV. As both target gases reach the same cutoff for this input energy, this suggests that plasma effects only have a minimal influence on the driving field propagation for this high attenuation case.

Besides the discussed influence on the cutoff, the pulse energy also has a strong impact on the overall HHG yield. For both gases the highest yield is reached at the highest pulse energy, whereby the highest yield for Helium (reached at 8 bar) is approximately 10 % of the highest yield in Neon (reached at 4 bar). Increasing the attenuation by switching to ND0.1 leads only to a minor

yield-drop of 10 % in Neon but to a more significant drop of 25 % in Helium. A further attenuation increase using ND0.2 leads to an order of magnitude decrease in yield for both cases.

1.3 In-situ waveform characterization

The driving waveforms are characterised in-situ using the TREX technique[1]. At each optimal gas target position a TREX scan is performed. In order to avoid distortions due to ionisation the scans are taken using the ND0.3 in Helium at 1 bar backing pressure. These precautions ensure that the measured waveforms closely resembles the ones in vacuum at the target position.

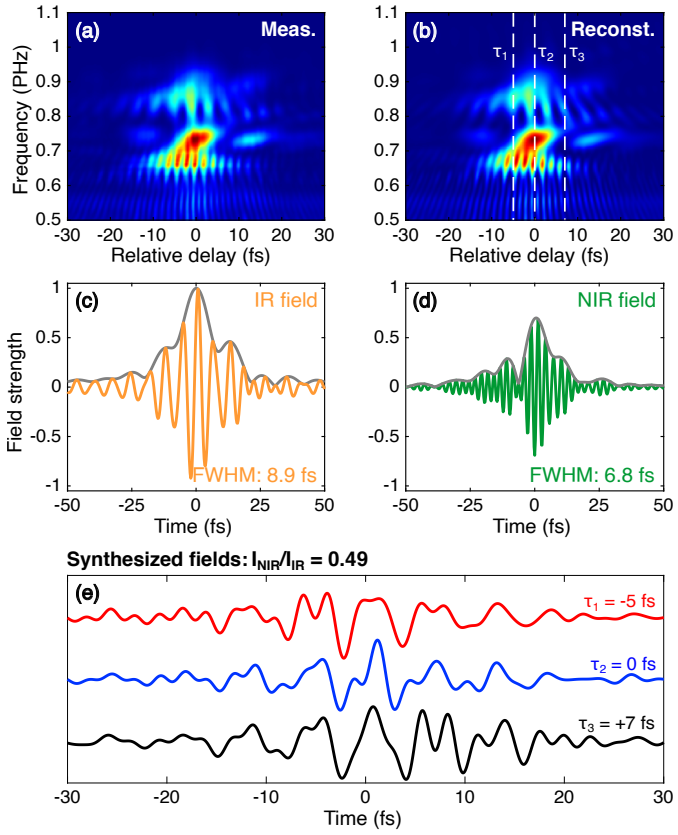

Figure 2: **TREX measurement for in-situ waveform characterization.** (a) Measured and (b) reconstructed TREX trace at the best gas target position z_{PM} = 1.5 mm for He at 1 bar using ND0.3. (c, d) Reconstructed IR and NIR fields (coloured) and their temporal envelopes (gray). The intensity FWHM durations are indicated. (e) synthesised waveforms resulting from the combination of the NIR and IR pulses at the indicated relative delays (white dashed lines in panel b).

The TREX signal, which extends down to 230 nm, is guided out of the vacuum system using UV-enhanced aluminium mirrors. To separate the strong copropagating fundamental from the nonlinear χ^3-signal, the beam is spatially dispersed using a pair of UV fused silica prism. The

filtered nonlinear signal is then recorded using a comercial grating spectrometer[1].

Figure 2 shows a TREX scan and the reconstruction result measured at the position, which is optimal for helium with the ND0.2 filter. The good agreement between measured and reconstructed trace, where even small features are well reproduced, demonstrates good convergence of the reconstruction algorithm. The reconstructed pulse durations are about 7 fs for the NIR and 9 fs for the IR with an NIR to IR energy ratio of 0.49. The central wavelengths of the reconstructed NIR and IR pulses are approximately 0.84 μm and 1.80 μm. The TREX method reconstructs both pulses including their relative- and absolute-phase as well as their precise time-zero given by the position where their centre of mass of their time-domain intensity envelopes overlap. Thus, the full set of synthesised waveforms for all delays and CEPs is known from one measurement as long as the phase lock is not broken.

The waveform characterisation was performed with the ND0.3 filter. In order to relate the reconstructed waveforms to the ones for the other ND filters, two factors need to be considered. First, the slightly different shapes of the transmissions curves for all filters not only lead to an overall change of input energy but also to a slight change of the overall spectral shape of the synthesised waveform, which includes also a change of the relative intensity ratio. Second, the slight thickness differences of the different filters on the order of a few tens of micrometers introduces a slight wavelength dependent phase change, which primarily manifests in an overall CEP and relative phase shift.

[1] USB2000+, (OceanOptics)

Table 3: **Intensity ratios for different ND filters.** NIR-to-IR intensity obtained from TREX waveform reconstructions at the optimal gas target positions (Table 2), and corrected values accounting for the transmission difference with respect to the ND0.3 filter (used in TREX measurements)

ND	He	Ne
0.0	0.35	0.33
0.1	0.37	0.33
0.2	0.42	0.46

To account for the first factor, the NIR to IR intensity ratio is corrected based on the known transmission ratio of both pulses listed in Table 3. The thickness differences on the other hand were characterised using a Michelson interferometer. Using the known refractive index of fused silica[2] the spectral phases of the reconstructed pulses were numerically adjusted to account for the measured differences.

1.4 Synchronisation of HHG Spectra with Single-Shot Synthesis Parameters

To analyse the connection between the driving waveform and the generated high-harmonic spectrum, we need to associate a specific waveform to each spectrum. To this end, we first determine the driving waveforms using the TREX method as described above. From this point on, the phase lock of the two synthesis parameters, relative phase and CEP of the waveforms, is maintained throughout all following measurements. The FPGA-based feedback unit of the synthesizer measures the two locking phases single-shot at 1 kHz, and streams this single-shot data over the network to the main data acquisition PC. Using the knowledge from the TREX scan, the relative phase and CEP

data can be translated to relative delay and CEP, which allows the reconstruction of each optical waveform. In order to synchronise this data with the acquired high-harmonic spectra the FPGA also records an electronic fire-signal, which is output by the SXR camera while it is integrating. The single-shot phase data is then averaged during each integration window. Since the fire-signal is also recorded single-shot, this procedure only averages exactly over those pulses contributing to the measured signal. The averaged locking phases are used to determine an effective driving waveform for every high-harmonic spectrum.

1.5 IR CEP scans

CEP scans of the IR field alone were used to maximise the HHG photon flux driven by the IR field. This allows for a direct comparison with the HHG yield when driven by the synthesised waveforms. Figure 3 shows CEP scans recorded in He and Ne, at different intensity levels of the single IR pulse.

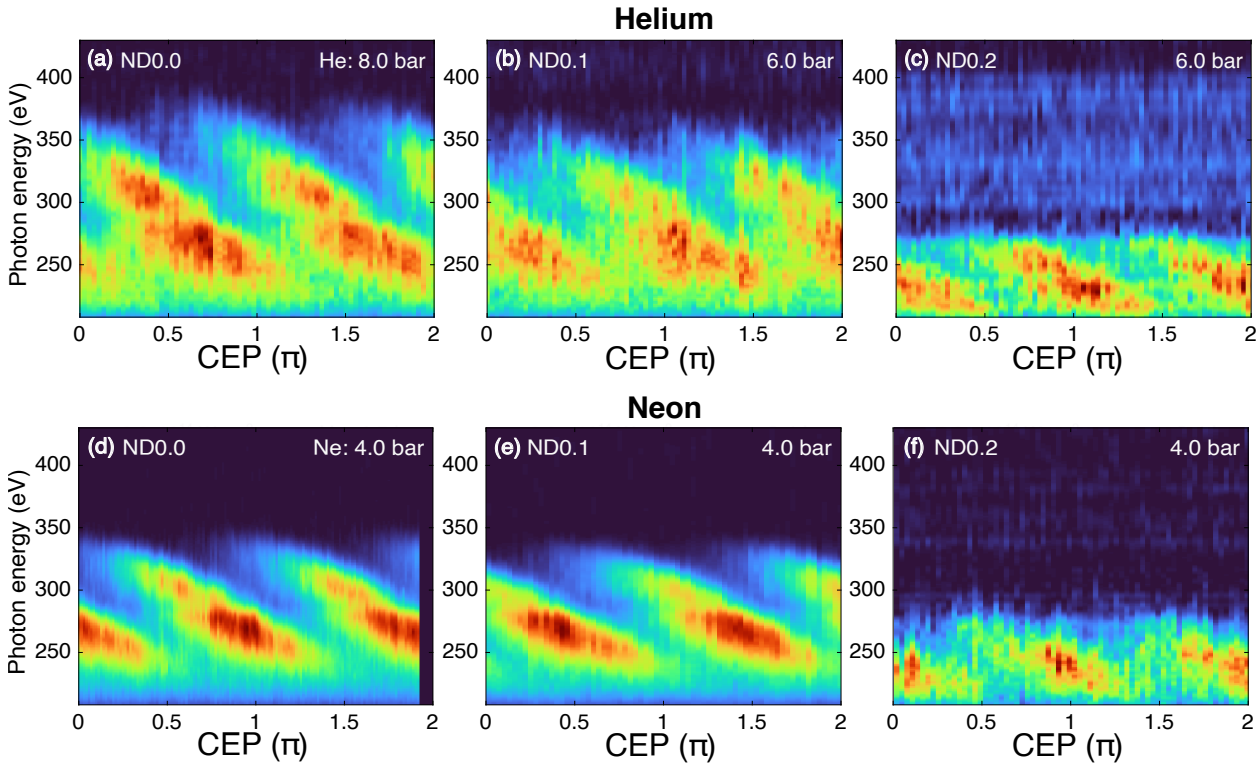

Figure 3: **Measured CEP scans in He and Ne driven by the IR pulse with varying ND filters.** HHG spectra as a function of CEP for ND filters: (a) 0.0, (b) 0.1, and (c) 0.2. The phase-matching conditions (pressure and target position) are specified in Table 2.

The resulting spectra exhibit a clear π-periodic CEP dependence of both cutoff and yield across the range of sampled peak intensities in both gases, indicating that the 1.5-cycle IR driver alone can generate IAPs. This CEP behaviour is consistent with previous studies in which IAP generation has been reported[3–5].

1.6 Relative delay scans

Figures 4–6 present relative delay scans recorded in helium at three intensity levels. For each level, the CEP is shifted by $\pi/4$, $\pi/2$, and π, with the latter serving as a consistency check. As observed for the ND0.2 and ND0.1 cases, at delays close to temporal overlap, the higher intensity of synthesised waveforms leads to the the highest cutoffs and photon yields. At ND0.0, however, the intensity near overlap leads to sufficiently high plasma levels that can abruptly distort the waveform already at positions near the entrance of the medium. As a consequence, the coherent addition of emissions with the highest energies is confined to the first portion of the medium, rather than over a large fraction of its length. In contrast, driving waveforms synthesised at larger delays, are less intense and the distortion is more gradual. This allows HHG to build up coherently over a longer propagation distance, allowing, in some cases, to produce brighter spectra than those generated near temporal overlap.

In certain delay intervals, the delay-dependent spectral modulation exhibits a characteristic "boomerang" pattern, whereas in others this feature is absent. When present, the boomerang modulation indicates that two consecutive half-cycles contribute to the emission, with one yielding a more energetic emission whose cutoff decreases with increasing delay and a second one at lower photon energies and increasing cutoff. The lower-cutoff emission usually originates from a neighbouring, later half-cycle and therefore experiences higher plasma fractions during propagation. At higher intensities, such as for ND0.1 and ND0.0 near temporal overlap, the reached plasma levels rapidly distort the field segment, suppress the emission and its coherent build-up. By contrast, the

preceding half-cycle propagates under lower plasma conditions, allowing its emission to accumulate coherently over a longer distance and reach a higher yield. As a result, the emission comes in the form of an IAP.

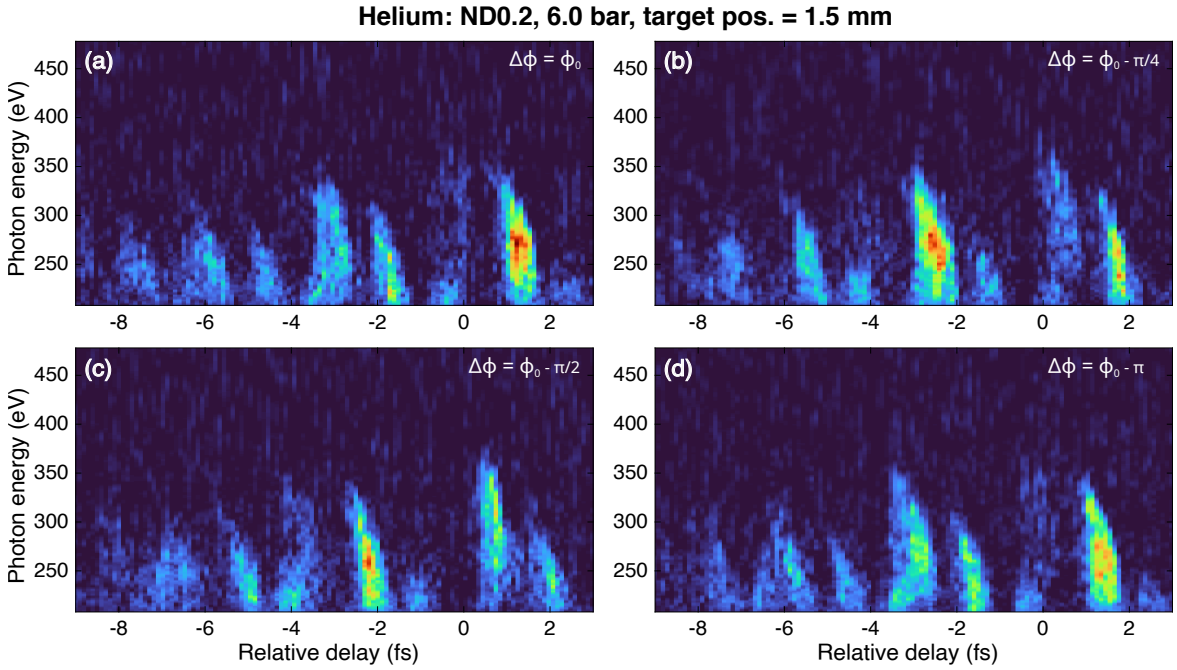

Figure 4: **Experimental relative delay scan in He with ND0.2 filter at various CEP shifts.**

When neon is used as the generation medium (Figs. 7–9), the delay-dependent behaviour differs from that observed in helium, aside from the generally reduced harmonic cutoffs, which rarely exceed ~ 350 eV. Owing to its lower ionisation potential, neon reaches significant plasma levels at lower intensities. At the lowest attenuation levels (ND0.0 and ND0.1), in contrast to the helium case, the most intense signals and higher cutoffs do not appear near delay zero, but rather a "depletion" region appears, spanning relative delays from approximately -13 to $+3$ fs, in which essentially no HHG signal above 200 eV is detected. In this delay range, the dominant cycle of the synthesised waveform remains sufficiently intense that it undergoes rapid plasma-induced

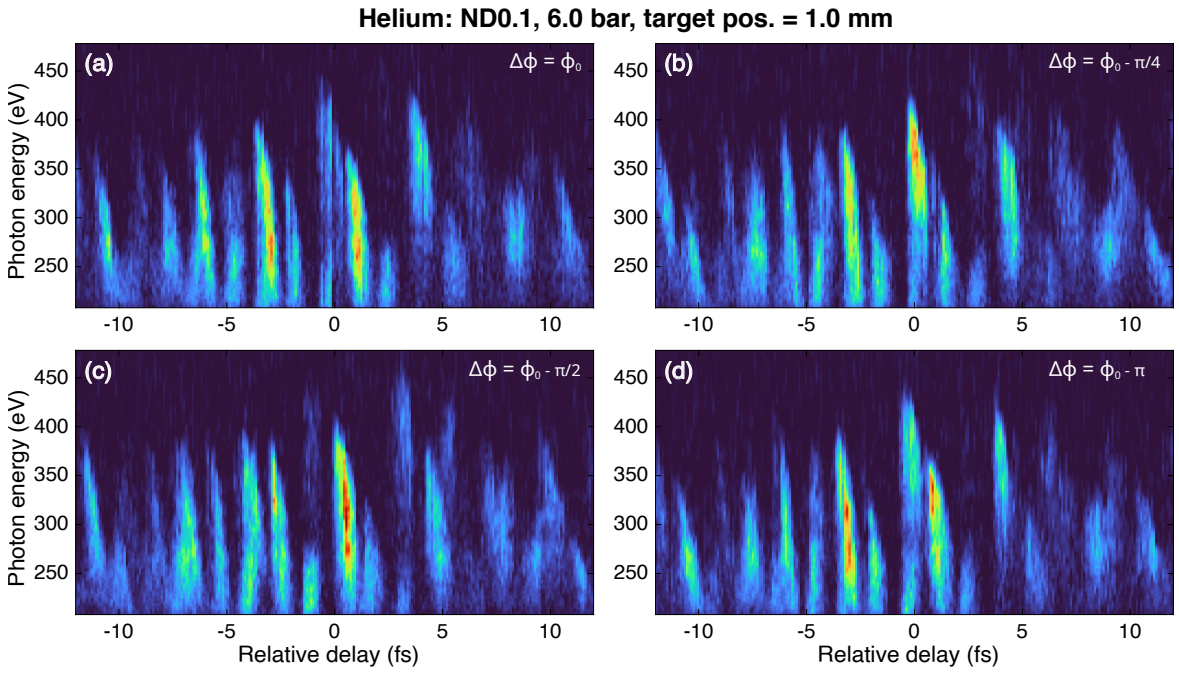

Figure 5: **Experimental relative delay scan in He with ND0.1 filter at various CEP shifts.**

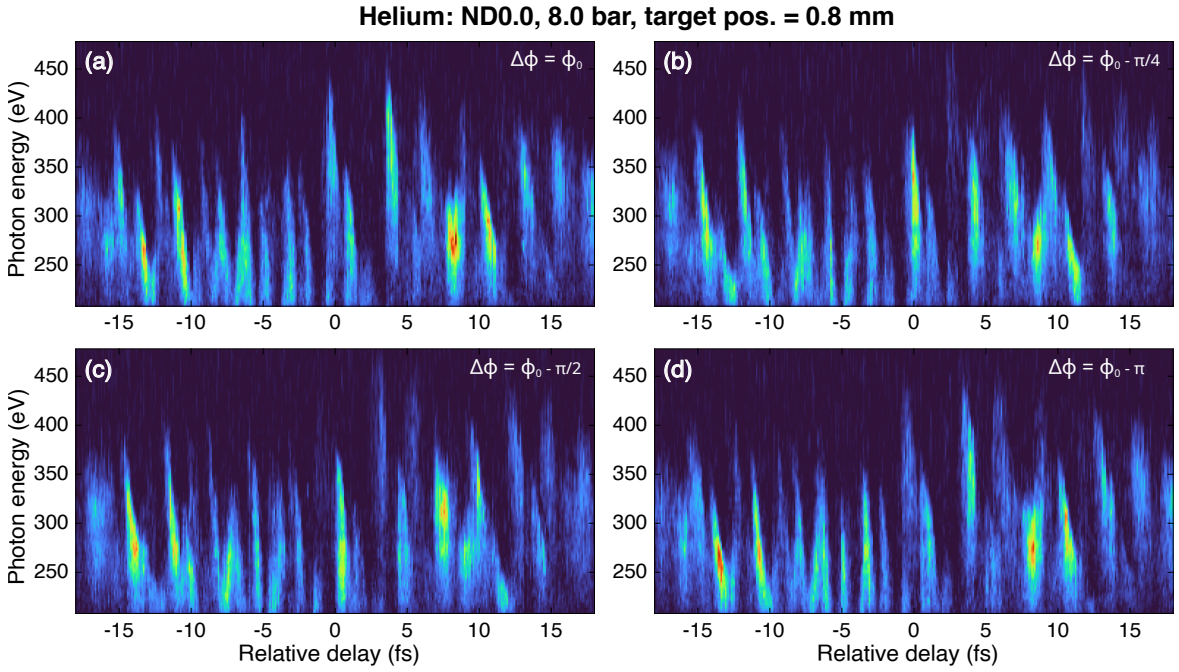

Figure 6: **Experimental relative delay scan in He with ND0.0 filter at various CEP shifts.**

distortion upon entering the medium, preventing sustained generation and coherent build-up of >200 eV emissions . By contrast, this depletion region is absent at the highest attenuation level (ND0.2). In this case, HHG emission originating from a single half-cycle persists across nearly the entire scanned delay range, with an enhanced yields near temporal overlap. The presence of a single dominant half-cycle contribution indicates that even at this reduced intensity, plasma formation is sufficient to suppress emission from neighbouring half-cycles leading to secondary emissions, thereby facilitating IAP generation. These neon scans highlight how plasma effects constrain the shortest and most intense waveforms synthesised near zero delay, limiting efficiency gains in the water window and shifting optimal generation toward lower photon energies.

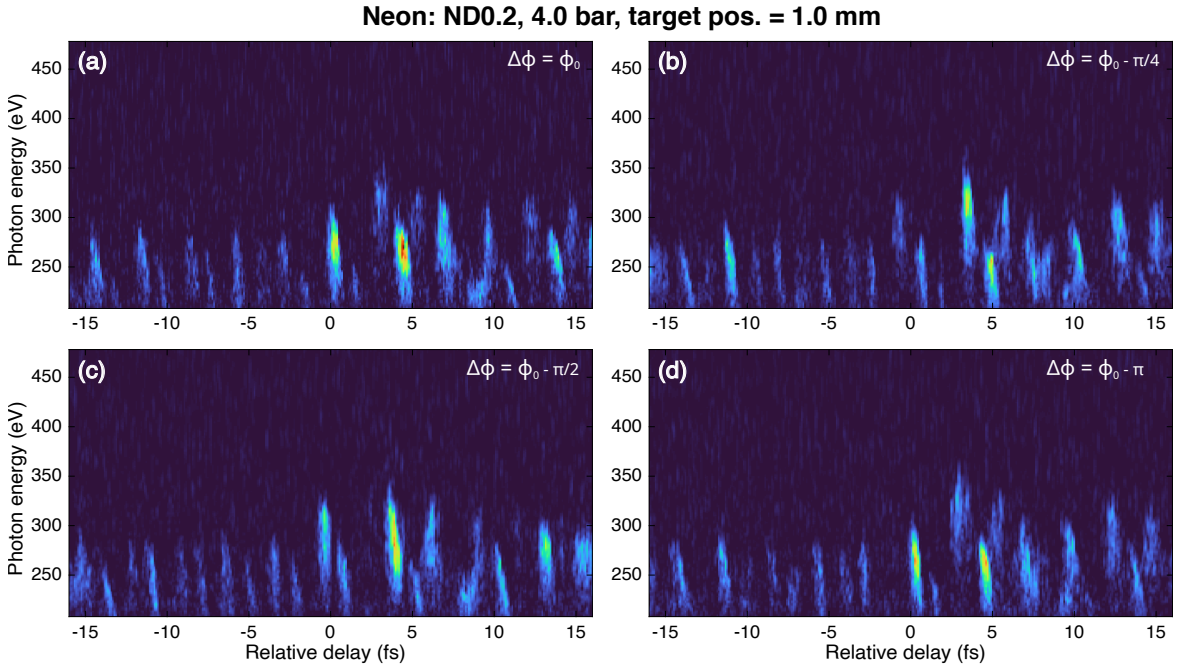

Figure 7: **Experimental relative delay scan in Ne with ND0.2 filter at various CEP shifts.**

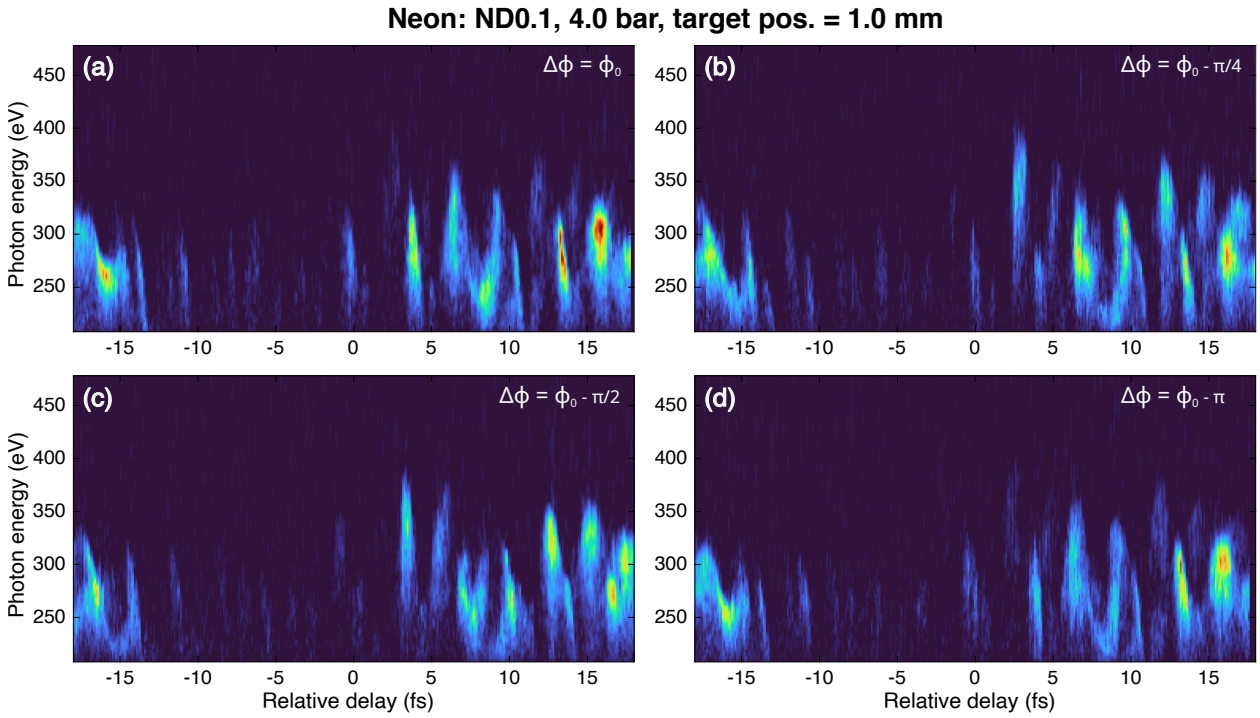

Figure 8: **Experimental relative delay scan in Ne with ND0.1 filter at various CEP shifts.**

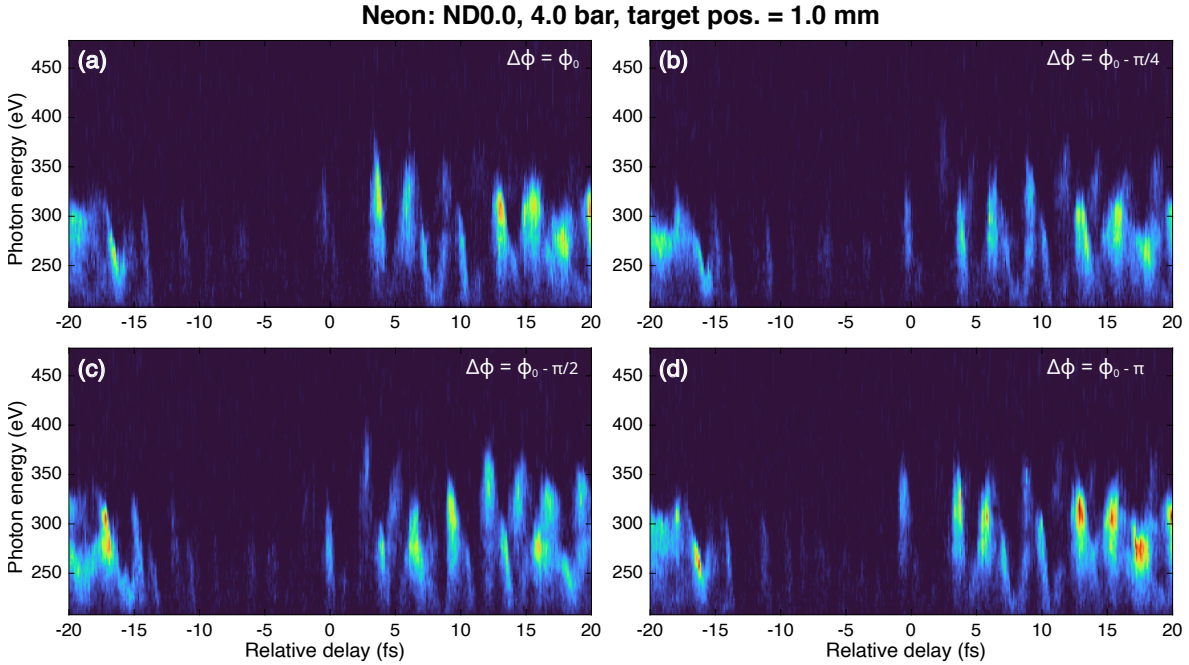

Figure 9: **Experimental relative delay scan in Ne with ND0.0 filter at various CEP shifts.**

1.7 Absolute photon flux measurement

The measurement of the soft X-ray photon flux is based on the signal recorded by a calibrated photodiode. This signal is used to calibrate the intensity axis of the CCD-based spectrometer measurements. Once calibrated, the photon flux for a specific energy range can be computed from CCD signals.

Since the photodiode is silicon-based, measurements are performed using the IR pulse only, with its spectrum ranging from 1.2 μm to 2.2 μm, instead of the NIR pulse, which spans 0.65 μm to 1.1 μm, as the NIR light would be absorbed by the silicon detector, complicating the distinction between the signals generated by soft X-ray light and optical light. During the measurement, all other light sources in and around the beamline are blocked or turned off, including pressure gauges (which have a hot filament that could emit light reaching the photodiode) and infrared light from closed-loop stages. Any potential reflections inside the HHG chamber are also blocked. Additionally, to measure within the water window, a combination of Al and Cu filters is used. This combination ensures that neither optical light nor low-order harmonics in the vacuum UV nor in the EUV range reaches the detector.

Figure 10 exemplifies the calibration measurements performed using this methodology. For this measurement HHG is driven using the IR pulse while its CEP is swept fast over a full period multiple times in order to record a CEP-averaged signal. This averaging over all CEP values prevents fluctuations in photon flux that might arise from the IR field being at a specific but random passively stable CEP. The generated emission is recorded by both the CCD and the photodiode.

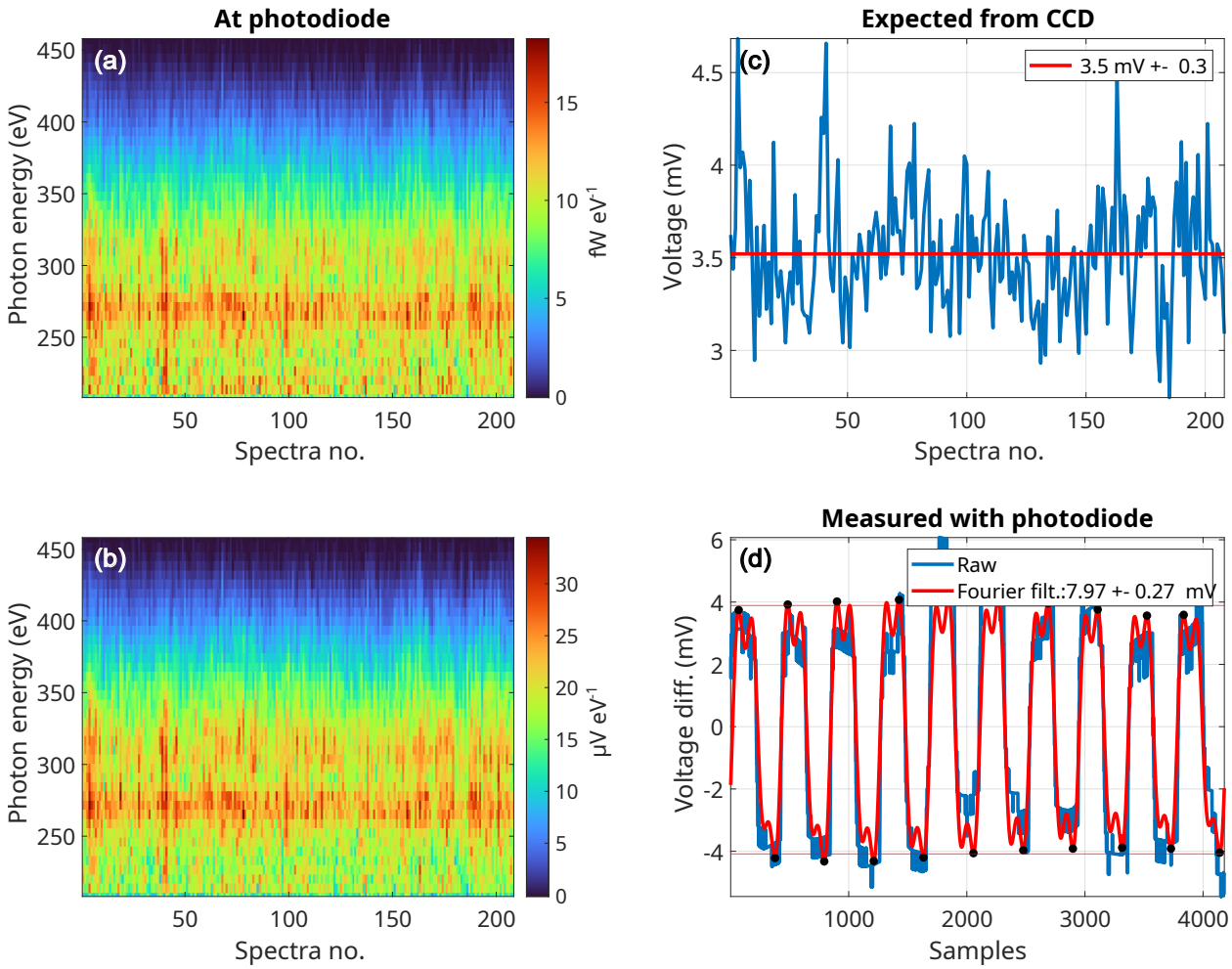

Figure 10: **CCD spetrometer calibration.** (a) Power spectral density inferred from the CCD measurement at the photodiode position. (b) Estimated voltage signal after accounting for photodiode responsivity (Fig. 1) and amplifier gain. (c) Integrated voltage signal with mean value plotted as a red line. (d) Voltage signal measured with the photodiode after background subtraction.

Analysis of the CCD-based measurement The number of incident photons on the CCD detector per eV, per second is given by:

$$n_{\text{CCD}}(\omega) = \frac{S_{\text{CCD}}(\omega) \cdot \sigma}{\eta_{\text{QE}}(\omega) \cdot n_{\text{e-h}}(\omega) \cdot t_{\text{exp}}} \tag{1}$$

where, σ is the sensitivity in electrons per CCD count, S_{CCD} is the raw measured signal (in counts per eV), t_{exp} is the exposure time, η_{QE} is the CCD quantum efficiency and $n_{\text{e-h}}(\omega) = \hbar\omega/3.65\text{eV}$ (in electrons per photon) accounts for the photon energy dependent average number of generated electron-hole pairs per incident photon in a Si-based detector [6].

The expected photon flux at the position of the photodiode (located before the grating) is then given by:

$$n_{\text{PD}}(\omega) = \frac{n_{\text{CCD}}(\omega)}{\eta_{\text{g}}(\omega)} \tag{2}$$

This formula accounts for the grating efficiency η_{g} but neglects any other potential transmission losses such as the input slit before the grating. From $n_{\text{PD}}(\omega)$, the power spectral density, plotted in Fig.10a, is calculated as:

$$P_{\text{PD}}(\omega) = n_{\text{PD}}(\omega) \cdot (\hbar\omega). \tag{3}$$

Finally, to account for the photodiode's spectral response, $P_{\text{PD}}(\omega)$ is converted to a voltage signal using the photodiode's known responsivity curve η_{PD} and the amplifier's transimpedance R of 10 GΩ. This converted signal is shown in Fig.10b. The integration of this signal over photon energies yields the photodiode voltage estimated via CCD measurements

$$V_{\text{est.}} = \int_0^{+\infty} P_{\text{PD}}(\omega) \cdot \eta_{\text{PD}} \cdot R \, d\omega \ , \tag{4}$$

Analysis of the photodiode-based measurement The calibration measurements of the responsivity of our photodiode was performed at beamline PO4 at PETRA III. The voltage signal generated by the soft X-ray radiation, V_{PD}, obtained with the following methodology is considered our most reliable reference for determining the HHG efficiency or photon flux. The measurement method consists of repeatedly inserting and removing a glass plate from the beam path to distinguish the soft X-ray signal from the optical background and account for a drifting offset of the readout circuit. This creates a time-varying pattern in the photodiode voltage, as shown in Fig.10d. By applying a Fourier filter, which selects only harmonics at frequencies associated to the periodic in/out movement of the plate, other residual sources of noise are removed and the voltage oscillation amplitude is determined.

CCD calibration factor The calibration factor (α), which accounts for any unknown further losses and discrepancies (i.e. losses on the input slit, imperfect XUV gratings, etc.), is given by the ratio between the measured photodiode voltage V_{PD} and the estimated voltage from the CCD measurement ($V_{\mathrm{est.}}$). The determined calibration factor for this particular example is:

$$\alpha = \frac{V_{\mathrm{PD}}}{V_{\mathrm{est.}}} = \frac{8.0 \pm 0.3\mathrm{V}}{3.5 \pm 0.3\mathrm{V}} = 2.3 \pm 0.2 \ . \tag{5}$$

For measurements presented in the main script, the calibration factor was $\alpha = 2.7 \pm 0.6$. This variability, again, stems from other non-accountable input coupling losses.

1.8 Efficiency measurements

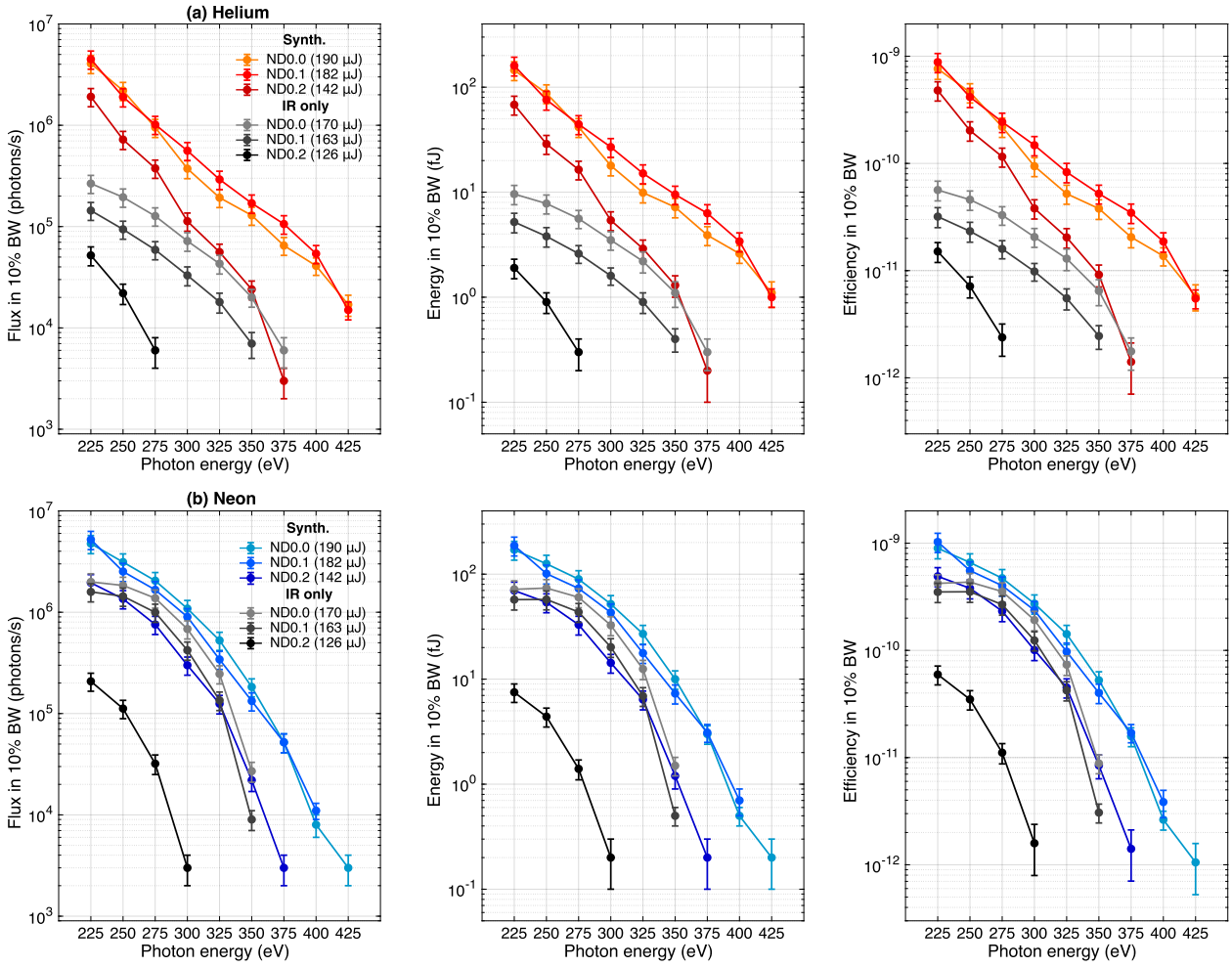

Figure 11: **Measured absolute HHG yield and efficiency in He and Ne with IR-only and synthesised fields.** Photon flux, energy, and efficiency ($E_{\text{out}}/E_{\text{in}}$) within a 10% bandwidth for (a) helium and (b) neon. Values represent the HHG source, produced by either the IR-only field (gray) or synthesised fields (coloured) at all attenuation levels (ND0.0-0.2), with corresponding beam energies shown. The IR-only values represent the maximum flux from CEP scans, while the synthesised field values represent the maximum flux achieved across four delay scans at different CEP shifts (0, $\pi/4$, $\pi/2$, and π; see Fig. 12).

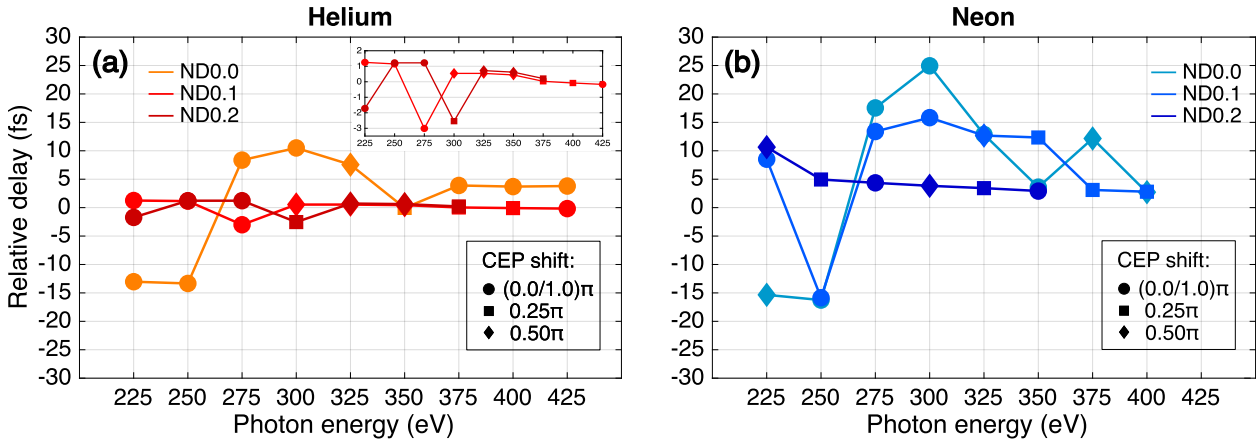

Figure 12: **Extracted waveform synthesis settings for optimised HHG yields in He and Ne.** Relative delays and CEP values (0, $\pi/4$, $\pi/2$, π) for the synthesised waveforms that led to the highest yields (shown in Fig. 11) at all attenuation levels (ND0.0-0.2) in (a) helium and (b) neon. CEP markers: circles for 0 and π, squares for $\pi/4$, diamonds for $\pi/2$. The inset in (a) provides a zoomed view of the relative delay axis.

2 On-axis macroscopic modeling of HHG

Simulating the macroscopic effects of HHG in the high intensity and high gas pressure regime is crucial to understand the mechanisms leading to the experimental observations. An exhaustive parameter search scanning all driving waveforms, gas pressures and gas target positions using a full four-dimensional (3 spatial and time) model by far exceeds computational resources. We thus opted to use an on-axis method, following Refs.[7,8], to simulate the driving waveform propagation and macroscopic build-up of HHG. This reduced model is significantly less computationally demanding and thus allows us to perform simulations for the complete set of experimentally used

parameters as well as further experimentally uncharted parameter regions. In order to describe the observed effects accurately one needs to include a focusing term for the propagation of the driving waveform; when using a description in three spatial dimensions this term is included naturally, in our reduced on-axis description this term needs to be added manually, which will be described in the following.

The general procedure to calculate the macroscopically observed HHG radiation for one specific choice of macroscopic parameters (gas target position, gas pressure, driving waveform shape and intensity) includes the following steps:

1. Nonlinear propagation of the driving waveform through the spatially varying gas target
2. Calculation of the time-dependent single-atom high-harmonic dipole moments at each axial position
3. Propagation of the harmonic radiation to the end of the gas target and coherent summation of all contributions
4. Projection of the calculated high-harmonic field to the far-field

In this approach the back action of the harmonic field on the driving field is neglected, decoupling the propagation of the driver and the harmonics. This approximation is justified since the harmonic intensity is many orders of magnitude lower than that of the driving field[8].

2.1 Optical driving field propagation

In order to propagate the driving field through the medium, we consider the influence of the neutral atomic gas and generated plasma as well as the geometric focusing of the driving beam. We use the Slowly Evolving Wave Approximation (SEWA), which is valid for pulse durations close to the single-cycle regime [9]. In this framework the on-axis propagation equation for the electric field in the reference frame of the speed of light, $\widetilde{E}(\omega, z)$, is

$$\begin{aligned}\frac{\partial \widetilde{E}}{\partial z}(\omega, z) = i\Big[k(\omega) - k_n(\omega, z)\Big]\widetilde{E}(\omega, z) \\ + \frac{i}{2\omega c}\mathcal{F}\left\{\frac{\partial J_{\text{abs}}}{\partial t}(t, z) + \omega_{\text{p}}^2(t, z)\widetilde{E}(t, z)\right\} \\ - \frac{i}{2k}\,\nabla_{\perp}^2\widetilde{E}(\omega, r, z)\Big|_{r=0}\,.\end{aligned} \tag{6}$$

The wavenumber $k_n(\omega, z)$ describes the linear dispersion of the neutral atomic gas and depends on the local density of the medium $\rho(z)$. The density is calculated from the pressure profile $P(z)$ using the ideal gas law with an assumed temperature of 293.14 K. Under these assumptions the shape of the density and pressure profile is the same.

Plasma effects are calculated from the time-domain ionisation dynamics. The $\omega_{\text{p}}^2(t, z)\widetilde{E}(t, z)$ term describes the plasma dispersion and leads to a blue-shift. It includes the plasma frequency ω_{p}^2, defined as

$$\omega_{\text{p}}^2(t, z) = \frac{e^2\rho(z)\eta_e(t, z)}{\epsilon_0 m_e}. \tag{7}$$

This frequency is both time- and spatially-dependent due to the density profile and because the driving field is continuous deformed during the propagation. When considering the full transverse

evolution of the driving beam, this term would lead to plasma defocusing, which is however not described in our on-axis model. In addition to dispersion also the energy loss of the driving field due to the ionisation is included. The loss is described by the J_{abs} term in Eq.(6). It is given by

$$J_{\text{abs}}(t,z) = \rho(z)[1-\eta_e(t,z)]\frac{I_p w(|\widetilde{E}(t,z)|)}{\epsilon_0|\widetilde{E}(t,z)|^2}\widetilde{E}(t,z), \tag{8}$$

We now turn to the description of the beam focusing in our on-axis code. The synthesised beam in vacuum is modelled as the coherent sum of N Gaussian beams, one for each synthesised pulse, which are evaluated on-axis ($r=0$), $\widetilde{E}_j(\omega,z,r=0)=\widetilde{E}_j(\omega,z)$:

$$\widetilde{E}(\omega,z) = \widetilde{E}_1(\omega,z) + \widetilde{E}_2(\omega,z) + \ldots + \widetilde{E}_N(\omega,z). \tag{9}$$

The radial dependence of each beam is given by:

$$\widetilde{E}_j(\omega,z,r)_{Vac} = \widetilde{E}_j(\omega,z)_{Vac}\exp\left(-\frac{r^2}{w_j(z)^2}\right)\exp\left(-i\frac{kr^2}{2R_j(z)}\right) \tag{10}$$

We can thus express the on-axis $(r=0)$ field of the j-the constituent beam in vacuum as:

$$\widetilde{E}_j(\omega,z)_{Vac} = \frac{E_j(\omega)_{Vac}}{\sqrt{1+\hat{z}_j^2}}\,e^{i\zeta(\hat{z}_j)}\,, \tag{11}$$

in which $E_j(\omega)$ is the spectral representation of the j-th constituent pulse, and $\hat{z}_j=(z-z_0^j)/z_R^j$ is a normalized axial coordinate. Here, z_0^j is the focal position of the j-th beam, and z_R^j is its Rayleigh length evaluated at the beam's central wavelength. This implies that no spatiotemporal coupling is assumed, meaning that all frequencies within the spectrum of the j-th constituent pulse share the same Rayleigh length z_R^j. The geometrical phase is given by $\zeta(\hat{z}_j)=\arctan(\hat{z})$. For the off-axis description, $w_j(z)=\sqrt{\frac{\lambda z_R^j}{\pi}}\sqrt{1+\hat{z}_j^2}$ is the beam waist and $R_j(z)=z(1+\frac{1}{\hat{z}_j^2})$ is the radius of curvature.

With the definition of Eq.(10), it is possible to evaluate equation Eq.(6) under vacuum, which allows us to formulate an analytical expression for the effect of the focusing term on the on-axis field.

$$\frac{\partial \widetilde{E}_j(\omega,z)_{Vac}}{\partial z} = -\frac{i}{2k}\nabla_\perp^2\ \widetilde{E}_j(\omega,z,r)_{Vac}\Big|_{r=0} = \widetilde{E}_j(\omega,z)_{Vac}\,\frac{1}{z_R^j}\frac{(i-\hat{z}_j)}{(1+\hat{z}_j^2)} = \widetilde{E}_j(\omega,z)_{Vac}\,g_j \quad (12)$$

This term accounts for the variation of the intensity and geometrical phase of a focusing Gaussian beam, which will be derived in the following. All linear propagation phenomena do not alter the shape of the beam profile if only radially independent density profiles are assumed. Only a high refractive index could change the value of z_R relative to vacuum conditions. This is, however, not the case for propagation in noble gases even in the multi-bar pressures used in this series of experiments. The main nonlinear effects that are able to reshape the beam profiles and change the focusing are thus plasma defocusing and Kerr lens focusing. If these effects are negligible, and the focusing positions and Rayleigh lengths are unaltered we can describe the evolution of the on-axis field in the medium based on the previously derived result for the vacuum case since the following relation holds:

$$\frac{-\frac{i}{2k}\nabla_\perp^2\ \widetilde{E}_j(\omega,z,r)_{Vac}\Big|_{r=0}}{\widetilde{E}_j(\omega,z)_{Vac}} = \frac{-\frac{i}{2k}\nabla_\perp^2\ \widetilde{E}_j(\omega,z,r)_{prop}\Big|_{r=0}}{\widetilde{E}_j(\omega,z)_{prop}} = \frac{1}{z_R^j}\frac{(i-\hat{z}_j)}{(1+\hat{z}_j^2)} = g_j \quad (13)$$

Because each beam can have a different $\hat{z}_R^j$ value, the last term of Eq.(10) can be written as

$$-\frac{i}{2k}\ \nabla_\perp^2\widetilde{E}(\omega,z,r)\Big|_{r=0} = \sum_j^N -\frac{i}{2k}\ \nabla_\perp^2\widetilde{E}_j(\omega,z,r)\Big|_{r=0} = \sum_j^N g_j\widetilde{E}_j(\omega,z) \quad (14)$$

in the case where nonlinear crosstalk between the beams due to ionisation or cross phase modulation are negligible.

These approximations break down for high ionisation level and medium density and one can expect the simulations to become more inaccurate in these scenarios. For the used gas pressures this limit is far away for the case of the IR-only HHG and is approached only for the highest synthesised field strengths, as will be discussed when comparing with experiments.

2.2 Harmonic field propagation

The macroscopic buildup of HHG radiation in the medium is also calculated using the SEWA. The harmonic field is thus also expressed in the reference frame of the speed of light. For the harmonic field, focusing terms are not taken into account. Thus, the different divergence of the long and short trajectories is not considered[10] and both contribute to the resulting spectra. The equation describing the propagation of the harmonics is

$$\frac{\partial \widetilde{E}_h}{\partial z}(\omega, z) + i\left[k_n(\omega, z) - k(\omega) - i\frac{\alpha(\omega, z)}{2}\right]\widetilde{E}_h(\omega, z) = -\frac{i\omega}{2c\epsilon_0}\widetilde{P}_{\mathrm{NL}}(\omega, z) \tag{15}$$

The equation includes the linear dispersion and absorption due to the gas medium but does not account for the plasma since the harmonic frequency is much larger than the plasma frequency. Absorption is described by the z-dependent absorption coefficient $\alpha(\omega, z)$, which depends on the gas density $\rho(z)$. The driving term on the right-hand side depends on the nonlinear polarization, which is derived from the single-atom dipole moment $d_h(t, z)$.

$$\widehat{P}_{NL}(\omega, z) = \rho(z)\mathcal{F}\left\{[1 - \eta_e(t, z)] \cdot d_h(t, z)\right\} \tag{16}$$

We calculate the dipole moment using the result of the driving field propagation at each point in

time and space. Eq. (15) has the analytical solution

$$\widetilde{E}_h(\omega, z = L_{\text{med}}) = -\frac{i\omega}{2c\epsilon_0} \int_0^{L_{\text{med}}} \widetilde{P}_{\text{NL}}(\omega, z) e^{-i\left[k_n(\omega,z) - k(\omega) - i\frac{\alpha(\omega,z)}{2}\right]\left(L_{\text{med}} - z\right)} dz, \tag{17}$$

where L_{med} is the length of the medium.

2.3 Simulation post-processing

After the propagation of HHG radiation in the medium, it is necessary to account for the transfer function of the beamline in order to make direct comparisons with the experiment in the far-field. One can apply the transfer function, for example, to the single atom response at the position where the fields were characterised (Fig. 13 (b)). Already at this level there is a correspondence concerning which features appear in the experiment. However, it is necessary to fully propagate the driving field and the HHG to see which features are better phase-matched (Fig. 13 (c-e)). In Fig. 13 (c) and (e), averaging considering the experimental CEP (300 mrad RMS) and Delay (50 as) noise is also applied at the post-processing step. Fig.13 (e) shows that the fringes from Fig. 13 (c) disappear when long trajectories are filtered out in the buildup of HHG. Fig.13 (d) shows the output considering only short trajectories without the waveform noise for direct comparison with Fig.13 (b).

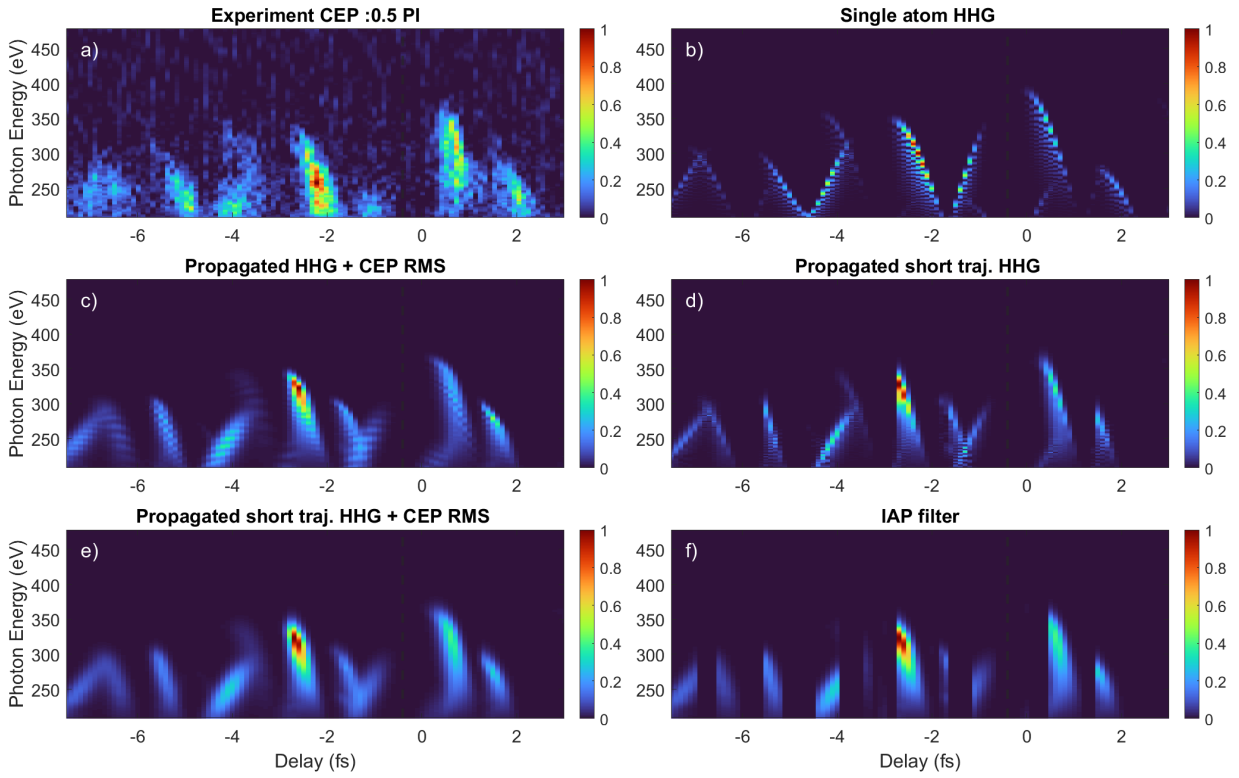

Figure 13: **Simulation post-processing:** (a) Experimental relative delay scan (e.g., ND02 intensity, CEP = -0.5pi). (b) Single-atom response relative delay scan. (c) 1D-propagated relative delay scan including waveform noise (d) 1D-propagated relative delay scan excluding long trajectories (e) 1D-propagated relative delay scan excluding long trajectories and including waveform noise. (f) same quantity as (e), however, filtering out emissions that do not correspond to isolated attosecond pulses. The synthesized field is at ND0.2 energy for all plots in this figure. (see Table1)

One challenge concerning 1D propagation of harmonics is how to separate short and long trajectories in the far field. Because the experiments were performed with characteristic Rayleigh lengths of the order of the medium dimensions ($L_{medium} \approx$ 1mm, $z_R^{IR} \approx$ 2mm), we can expect

that the harmonics do not diverge considerably during propagation in the medium. Hence, it is reasonable to coherently add the on-axis short-trajectory contributions. To exclude the long trajectories though, a filter is applied at each position of the propagation in the post-processing step. The filter acts on every attosecond burst produced by the driving field and applies a cos^2 decay of the emission in the time domain. The filter has 250as FWHM to ensure a smooth decay of the emission without introducing new frequencies to the attosecond burst due to nummerical artifacts. The filter's half maximum instant in time is adjusted to be at the instant of the cutoff emission.

Finally, to graphically exemplify how the IAP filter works for calculating the maximum flux in simulations, Fig. 13 (f) is a modified version of Fig. 13 (e) with emissions plotted only when an IAP is present. The HHG emission is considered an IAP in our simulations if the emissions of the other cycles above 200 eV have a peak intensity not exceeding 10% of the peak intensity of the main pulse. Graphically, it is very intuitive that intersection points between features that point to the left and right in the delay axis are excluded, because they correspond to emission under different half-cycles, leading to pulse trains. For Fig. 13 (f), the peak intensity after the beamline transfer function is considered for calculating the isolation degree of the pulses. However, in this study we are interested in the isolation degree already at the source, which is the kind of result shown in the main text and in section 2.11. Additionally, when calculating the maximum flux at a given photon energy for the simulations, it is necessary to ensure that the spectral component of interest is contained in the IAP and not in secondary emissions. Particularly at the source, where emissions at lower photon energies dominate, this is an even stricter demand for the IAPs.

2.4 Comparison with Luna.jl

The Luna code is able to simulate the free space propagation of optical fields in gaseous media.[11] Its on-axis output matches the results obtained with our 1D code Eq.(10) when the plasma term is neglected. This also means the same equations for the linear dispersion of materials are adopted in our propagation code. In addition, we have integrated the Tong-Lin ionisation model into the Luna code for simulating the plasma-induced propagation effects and third-order nonlinear effects were neglected. For the case of IR-only HHG, the final harmonic yield shows similar magnitude and the major differences are in the dependence of the harmonics as a function of gas cell position relative to the focus. This is caused by a very slight plasma defocusing effect. The direct photon-flux comparison between our code and Luna will be presented in Fig. 30. Figure 14 shows the comparison between codes for gas cell scans with the same driving field intensity and different pressures.

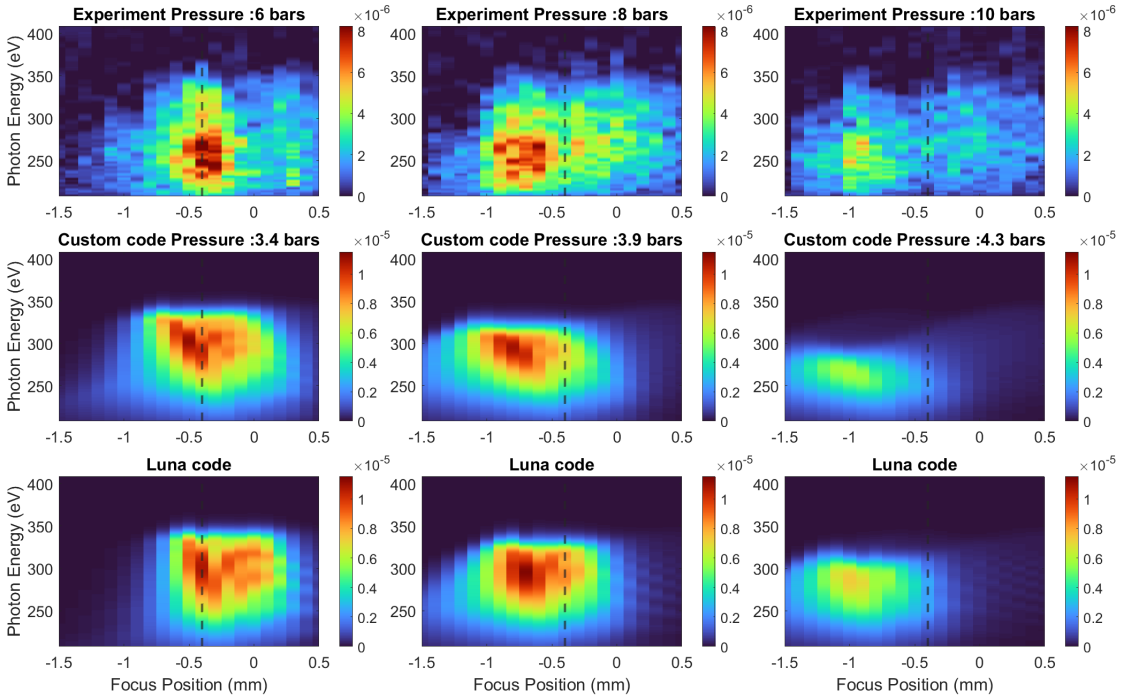

Figure 14: **Comparison between a full 1D propagation code and a mixed 2D optical 1D HHG propagation code** in the reproduction of experimental gas cell scans. The dashed line indicates the position under which the synthesised scans were performed. The IR-only field is at ND0.1 energy (see Table1).

2.5 Comparison with other ionisation models

For a brief comparison between ionisation models, we show the ionisation levels predicted in the focus of the 182 μJ (ND0.1) synthesised pulse for different models in He and Ne as a function of the relative delay between the two pulses. The reason for not choosing ADK for He,[12] is mainly because a model that consistently describes the ionisation levels for both gases was desired. This is the case for the Tong-Lin model,[13,14] that accounts for the barrier suppression regime in Neon,

which leads to considerably lower ionisation levels than ADK. Due to the extremely broadband pulses used and the various different central wavelengths that are obtained depending on which cycle is driving the ionisation and also on the synthesis parameters, the PPT model was not chosen for this work.[15] As in the case of ADK, it also yielded overestimated ionisation levels. A recently published model, Gasfir,[16] is able to provide a very good fit to TDSE results and does not require a central wavelength as input. The quasistatic Gasfir limit calculates ionisation levels slightly above the ones predicted by the Tong-Lin model for Helium, and shows very good agreement for Neon. A comparison of a RP scan with the same parameters as in Fig. 15 is shown for Tong-Lin ($\alpha = 7$) and Gasfir. Because it does not concern an order of magnitude change in the ionisation, the output is not considerably affected.

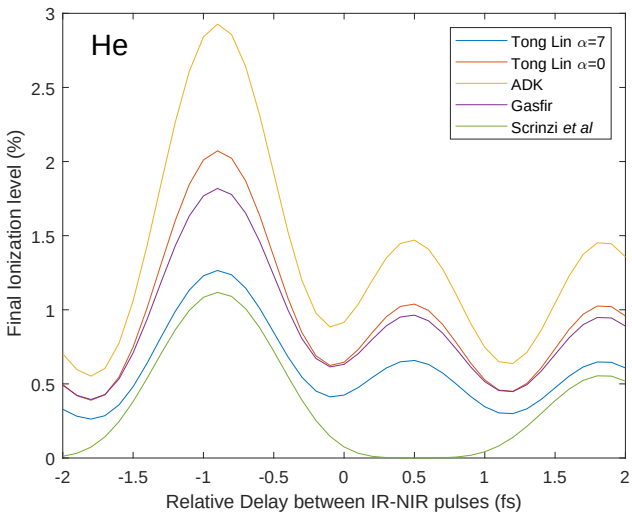

Figure 15: **Comparison of ionisation models in Helium** Different ionisation models are compared by plotting the the final ionisation level as a function of the delay between the two pulses. The model referred as Scrinzi *et al.* is what the Tong Lin $\alpha = 7.0$ model used as a numerical reference for the fitting.[17]

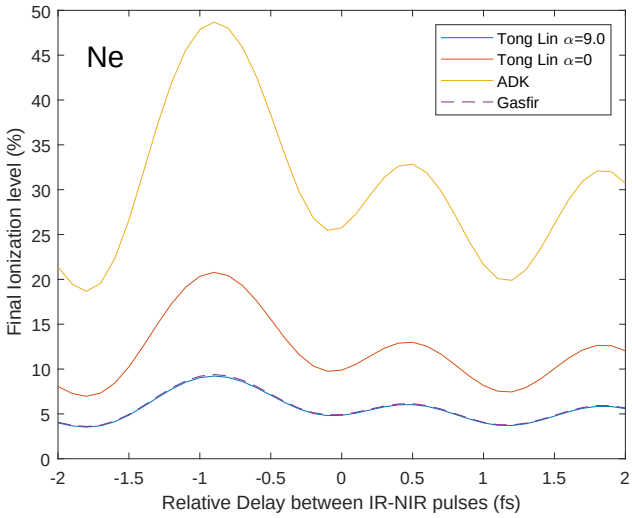

Figure 16: **Comparison of ionisation models in Neon** For the same fields as in Fig. 15, the ionisation levels predicted by different models for the case of Neon are plotted.

For the case of Helium and with the same propagation conditions, RP scans simulated with two different ionisation models are shown in Fig. 17. The ionisation level changes mostly the fine features of the HHG build-up.

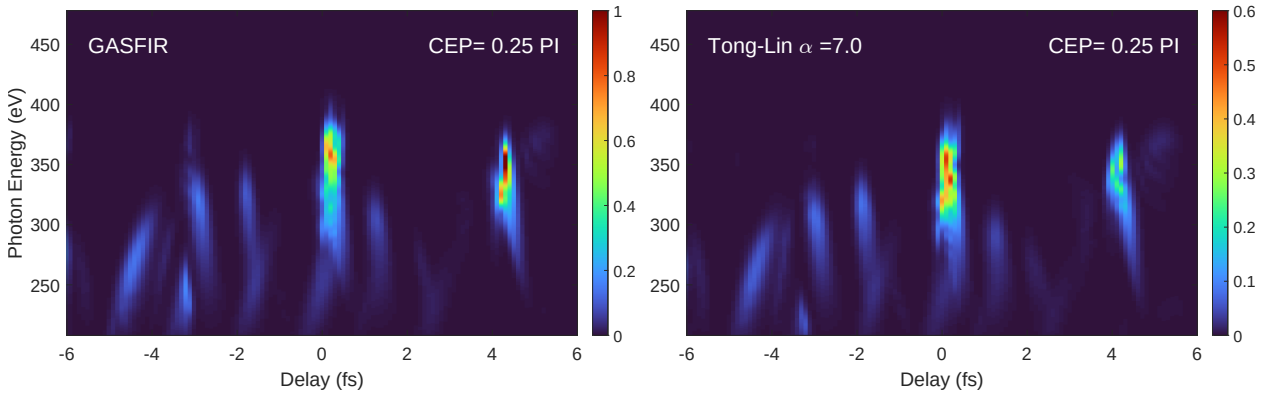

Figure 17: **Simulation of Rp scan for different ionisation models** For the same macroscopic conditions, $I_{IR} = \ 365TW/cm^2$, $I_{NIR} = 0.37 * I_{IR}$, $z_R^{IR} = 2$ mm, $z_R^{NIR} = 4$ mm and gas cell 2 (Figure 18), pressure 4.9 bars.

2.6 Gas cell scans

Different gas cell dimensions and Rayleigh lengths were tested to verify potential better agreement with the experiment. We observed very similar yields and behaviour as a function of gas cell position and pressure for various different conditions. Since our gas cell consists of a tube with 0.8 mm internal diameter and 1.0 mm external diameter with small 200μm holes, one attempt to describe the medium was a gas cell (GC1) with very short $\cos^2$ wings (0.1 and 0.2 mm) and a constant pressure region of 0.9 mm. Asymmetric wings were chosen because the laser drilling produces holes of slightly different size in each side of the gas cell. This kind of gas cell geometry was simulated in a previous work by Varoutis *et al.*[18]. It was shown, that the smaller the hole, the longer the wing, and vice versa. For Neon, we believe the holes were larger than for Helium, since the data was taken one day after Helium and slight degradations of the gas cell are likely

to have happened. These very short wings reproduce the data for Neon very well but do not very well with the data for He, even though the behaviour of HHG as a function of pressure does also agree very well with experiments. Another attempt was made by modelling the central feature of the gas cell scans with a 0.4 mm constant pressure region and 0.8 mm wings (GC2). This is also computationally more demanding because of the longer propagation distance (2 mm in total), however, yields qualitatively better results for Helium, as shown in Figure 18.

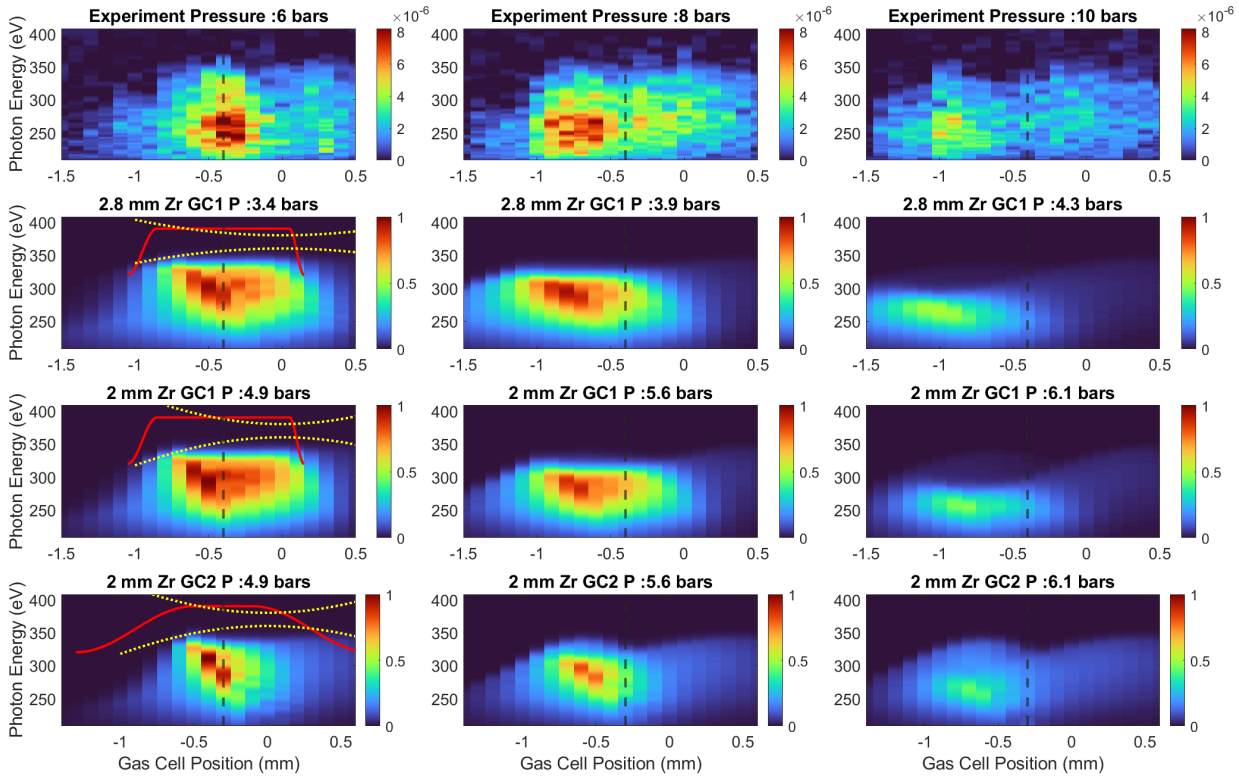

Figure 18: **Comparison of the use of different Rayleigh ranges (z_R) and gas cell shapes for He.** The focusing beam is indicated by a yellow dotted line and the gas cell is drawn in red at the position of more broadband and intense harmonic yield, also used for the CEP scans (dashed lines). The used energy in this case was ND0.1 (see Table1).

Other combinations of gas cell pressures and geometries are shown in Figure 19. When the gas cell dimension is considerably shorter than 1 mm, one can also observe the effect of a more narrow gas cell position range under which HHG is efficiently produced. This observation is also relevant for keeping the gas cell medium parameters close to the range of 1 mm FWHM and constant pressure region $\geq$ 0.4 mm.

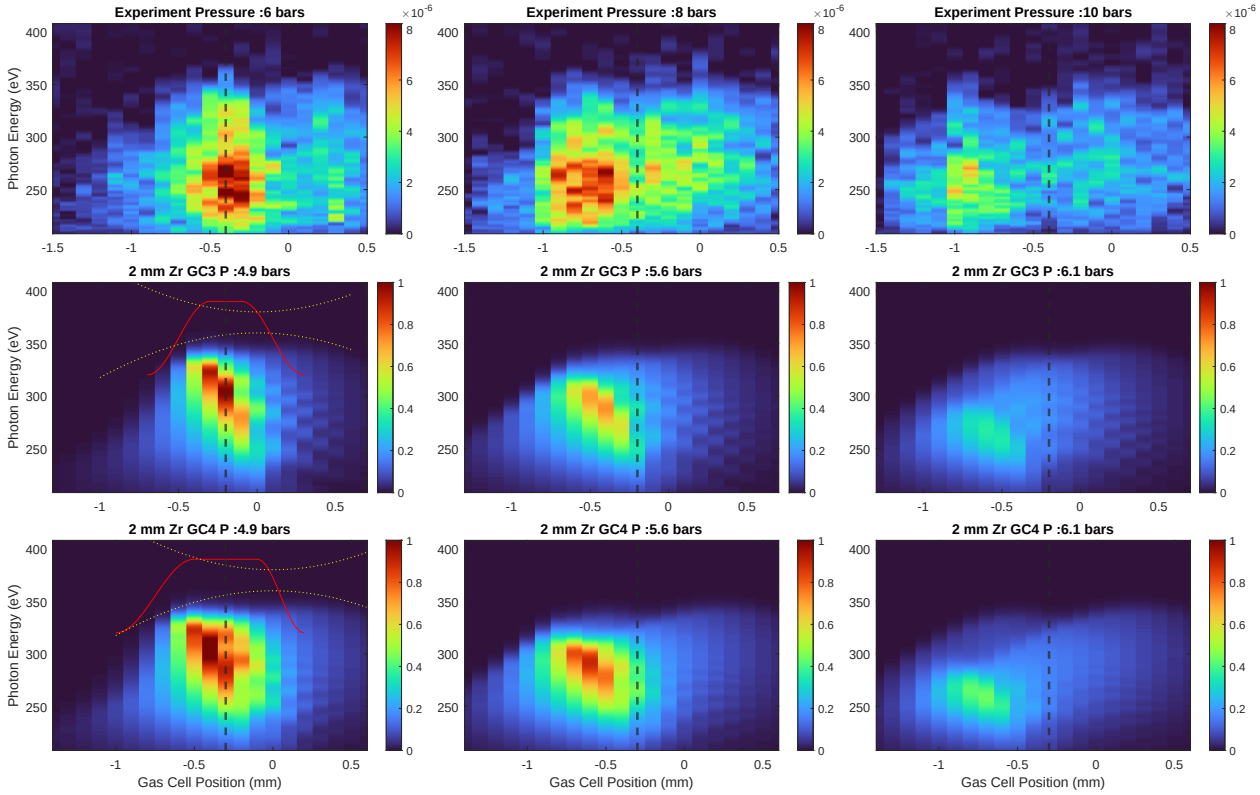

Figure 19: **Different gas cell profiles** For the same z_R = 2 mm, two different simulated gas cell scans at 3 different pressures are plotted against the experimental data. GC3 has 0.2 mm constant region and 0.4 mm wings. GC4 has 0.4 mm constant region and asymmetric 0.3/0.5 mm wings. The used energy in this case was ND0.1 (see Table1)

Finally, in Figs. 20 and 21, a full set of simulations for GC1 and $z_R = 2.8$ mm is presented for He and Ne. The parameters for the simulations are presented in Table 4.

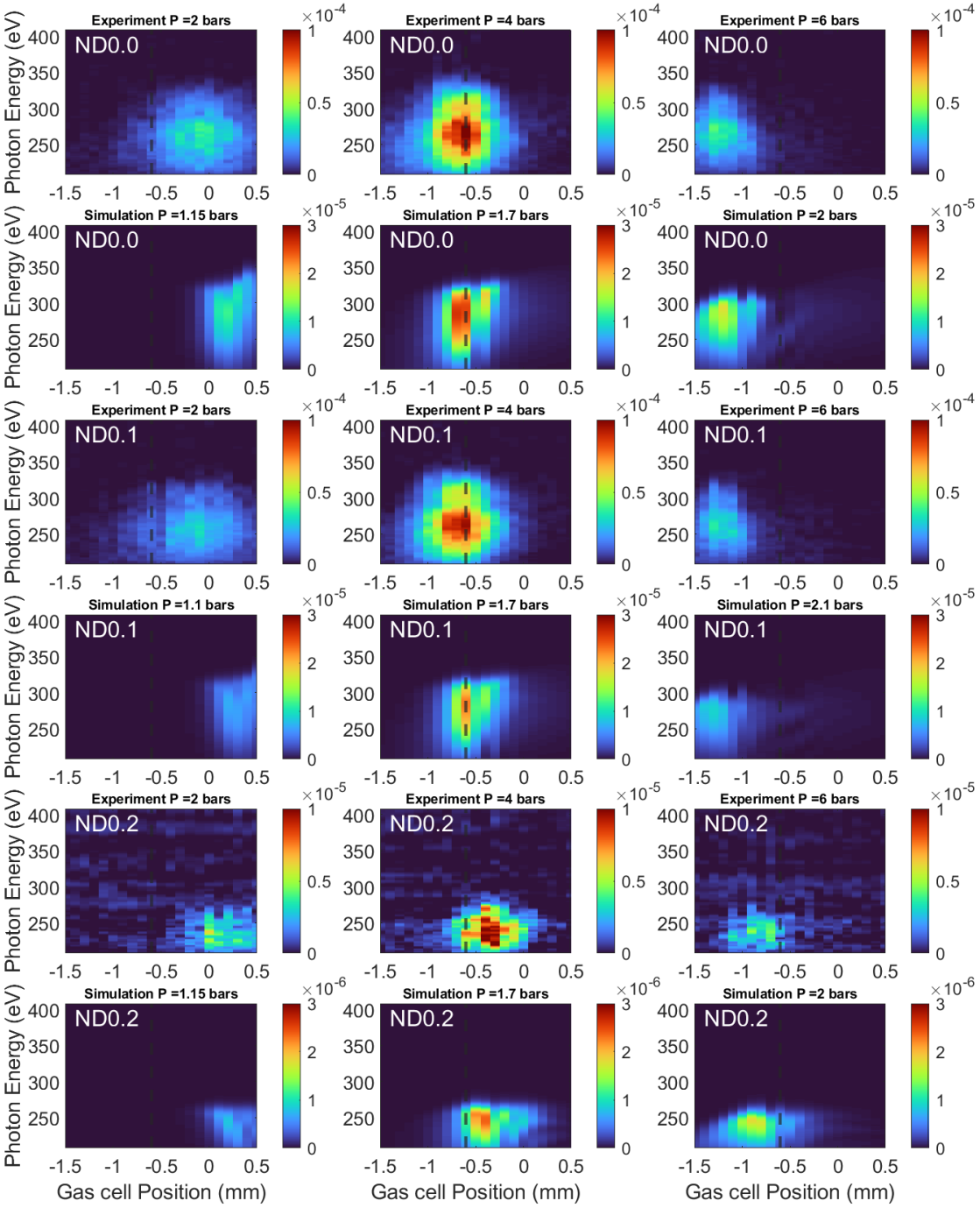

Figure 20: **Comparison between experiment and simulations with the Luna code for Neon gas cell scans.** The simulations were run with GC1 and $z_R = 2.8$ mm.

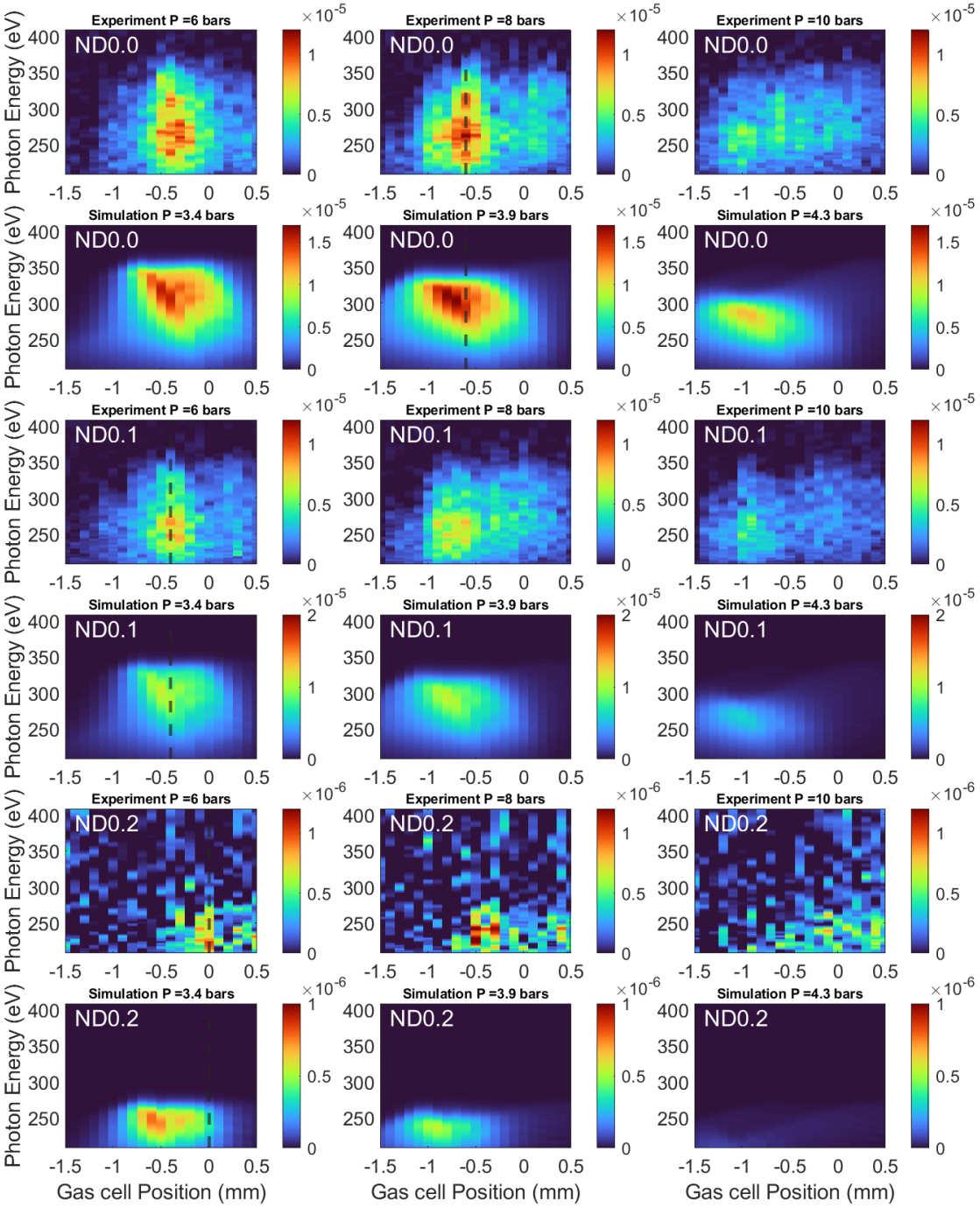

Figure 21: **Comparison between experiment and simulations with the Luna code for Helium gas cell scans.** The simulations were run with GC1 and $z_R = 2.8$ mm.

2.7 Simulation Parameters

With the determination of the macroscopic parameters using the gas cell scans, it is possible to fix parameters for simulating the experimental CEP and RP-CEP scans. The set of parameters used in the final simulations is shown in Table 4. An alternative set of parameters with GC2 (see Fig. 18) are shown in Table 5.

Table 4: Set of parameters used for the simulations with $z_R^{IR} = 2.8$ mm, $z_R^{NIR} = 5.3$ mm and GC1 (see Fig. 18). The focus position is defined relative to the center of the gas cell. The peak intensity is defined by the nominal value that would be achieved if the pulse was being focused in vacuum.

Common parameters		**Helium**		**Neon**	
ND	Peak Intensity (TW/cm^2)	Pressure (bar)	Focus pos. (mm)	Pressure (bar)	Focus pos. (mm)
0.0	380	3.9	0.5	1.7	0.6
0.1	365	3.4	0.4	1.7	0.6
0.2	281	3.4	-0.1	1.7	0.6

Table 5: Set of parameters used for the simulations with $z_R^{IR} = 2$ mm, $z_R^{NIR} = 4$ mm and GC2 (see Fig. 18). The focus position is defined relative to the center of the gas cell. The peak intensity is defined by the nominal value that would be achieved if the pulse was being focused in vacuum.

Helium

ND	Peak Intensity (TW/cm^2)	Pressure (bar)	Focus pos. (mm)
0.0	380	5.6	0.5
0.1	365	4.9	0.3
0.2	281	4.9	-0.2

2.8 CEP Scans

Comparison between experimental and simulated CEP scans for the conditions shown in Table 4.

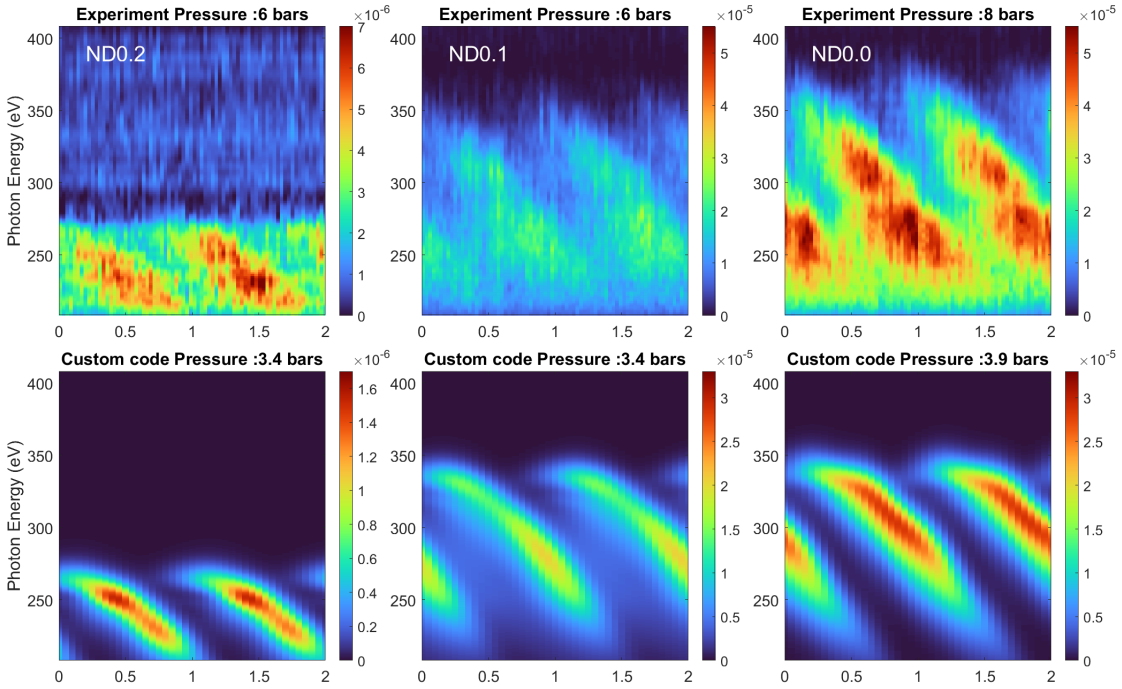

Figure 22: **CEP scans for Helium using the Luna code for the propagation of the IR field.**

Because of the low ionisation yields, the result is very similar for the simpler 1D code.

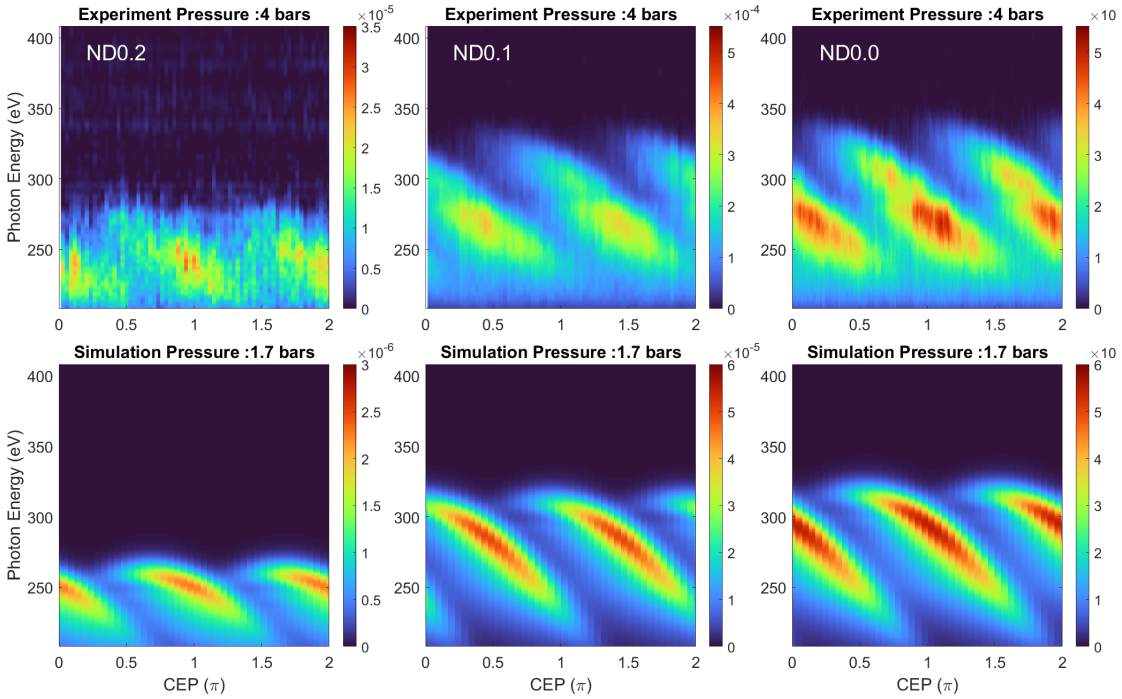

Figure 23: **CEP scans for Neon using the Luna code for the propagation of the IR field.** Because of the low ionisation yields, the result is very similar for the simpler 1D code.

2.9 Relative delay scans in Helium

Apart from the phase scans reported in the main manuscript, we recorded scans at various overall intensities (ND0.0, ND0.1, ND0.2) in Helium and Neon. This is justified by the stark increase of peak intensity around zero time delay between IR and NIR channel. On top of the delay scan with fine delay resolution (0.1 fs), a more coarse scan across the CEP is done (0.25 π). In Figs. 24-26 four plots of relative delay scans are displayed, each for a dedicated CEP. The precise CEP value is inferred from TREX measurements. The simulations shown were from the conditions indicated in Table 4.

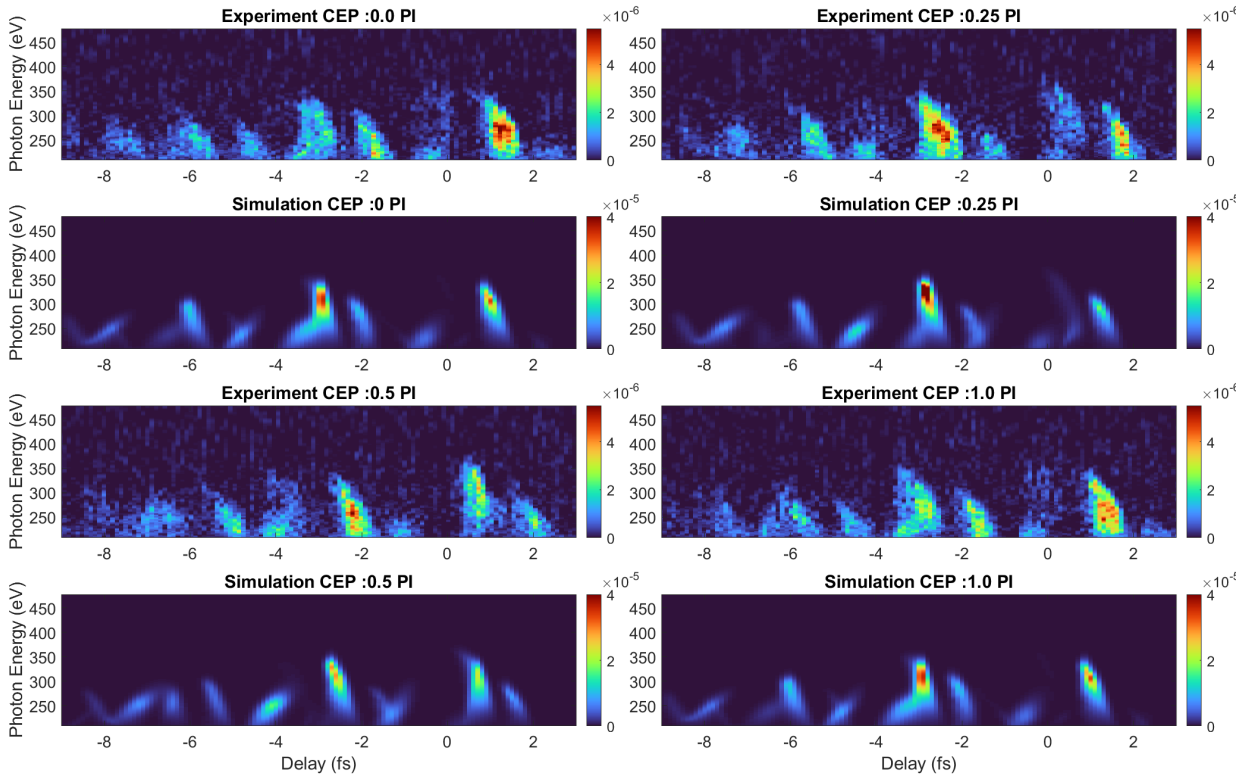

Figure 24: **Experimental and simulated delay scans in Helium** for 142 μJ synthesizer pulse energy (ND0.2).

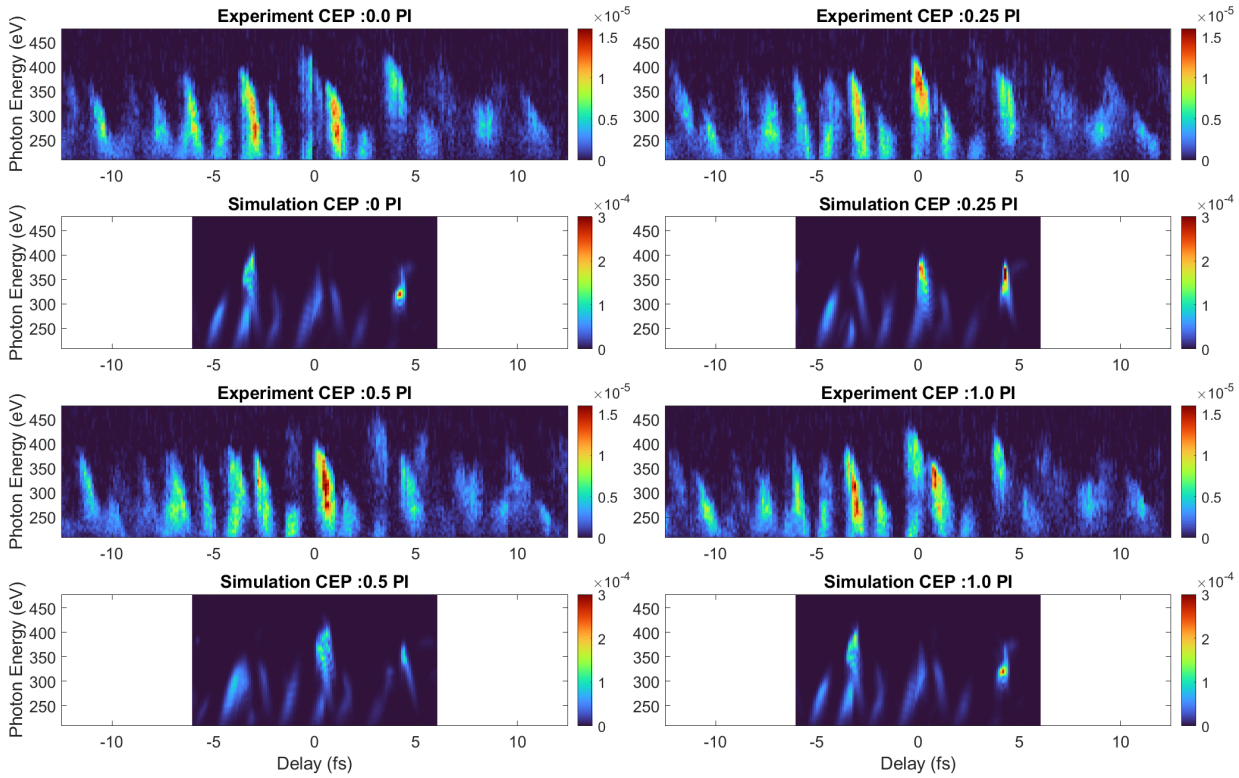

Figure 25: **Experimental and simulated delay scans in Helium** for 182 μJ synthesizer pulse energy (ND0.1).

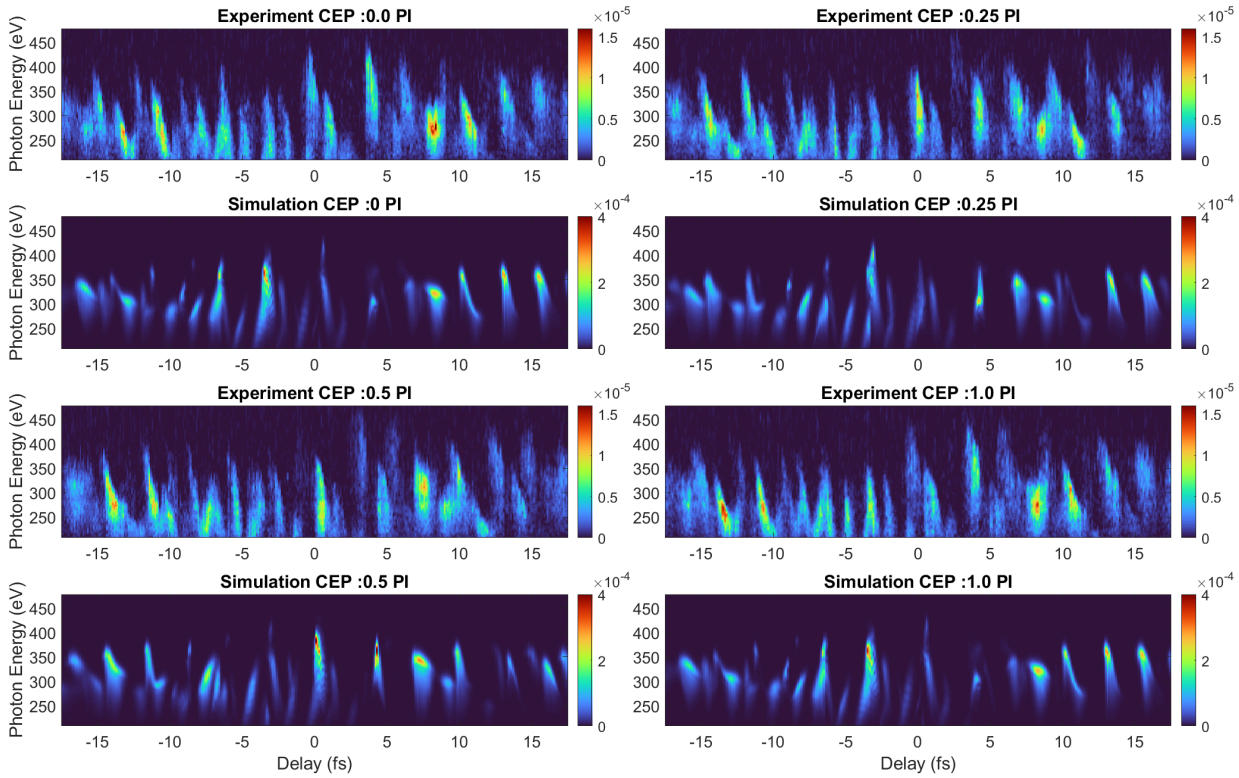

Figure 26: **Experimental and simulated delay scans in Helium** for 190 μJ synthesizer pulse energy (ND0.0).

2.10 Relative delay scans in Neon

All the simulations for delay scans in Neon were performed with the custom full propagation 1D code. Several continua are well reproduced both in shape and absolute yield. For the higher pulse energy scans (Figs. 28-29), there is a noticeable region of HHG depletion around time zero relative delay. This is caused by the very high peak intensities leading to a high ionisation of the medium that does not allow phase matching during propagation. For larger positive delays after the depletion region (>1 fs), a few waveforms demonstrate cutoff extension, as will be pointed out

in the flux analysis of Fig. 31.

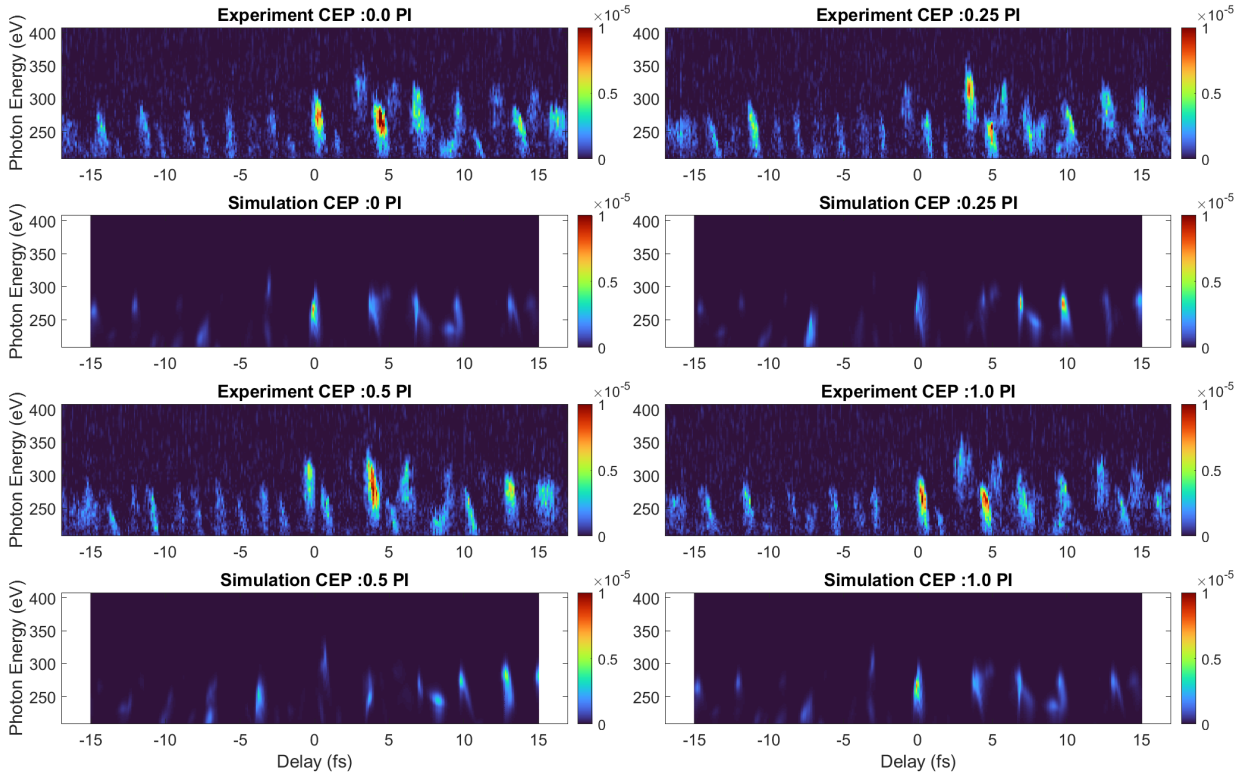

Figure 27: **Experimental and simulated delay scans in Neon** for 142 μJ synthesizer pulse energy (ND0.2).

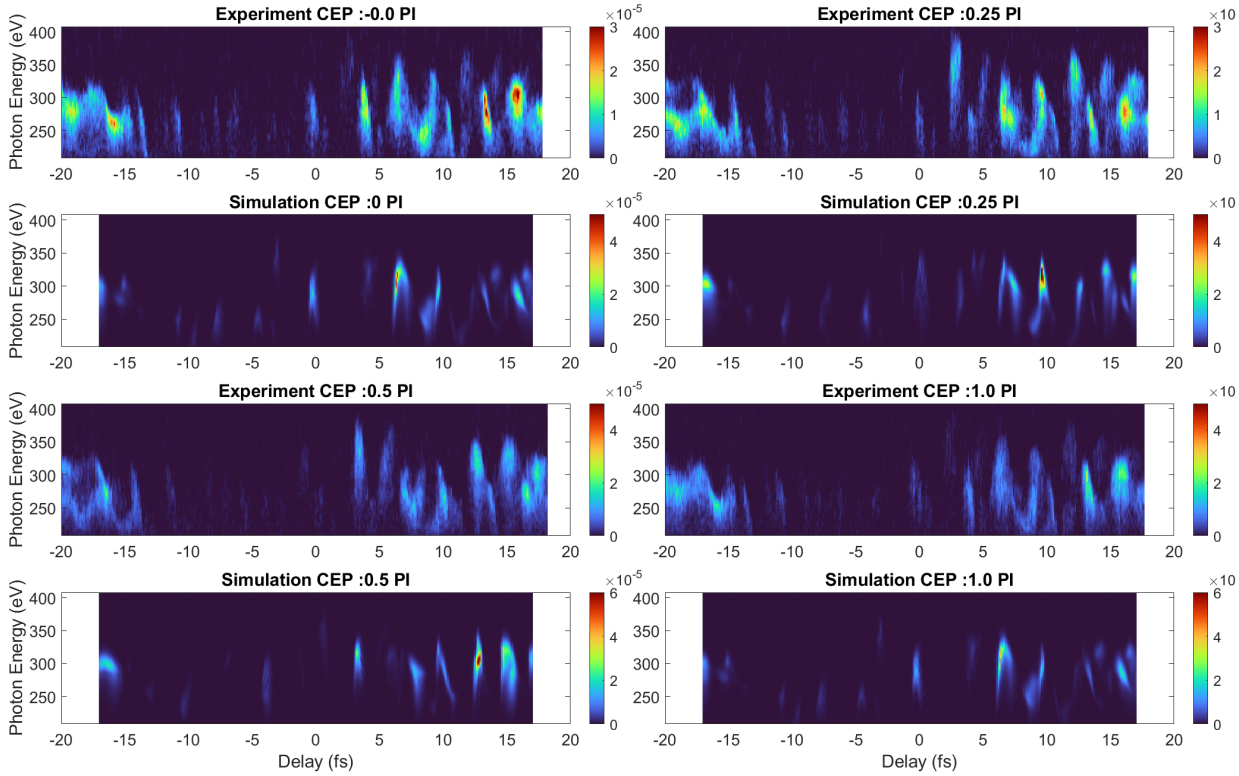

Figure 28: **Experimental and simulated delay scans in Neon** for 182 μJ synthesizer pulse energy (ND0.1).

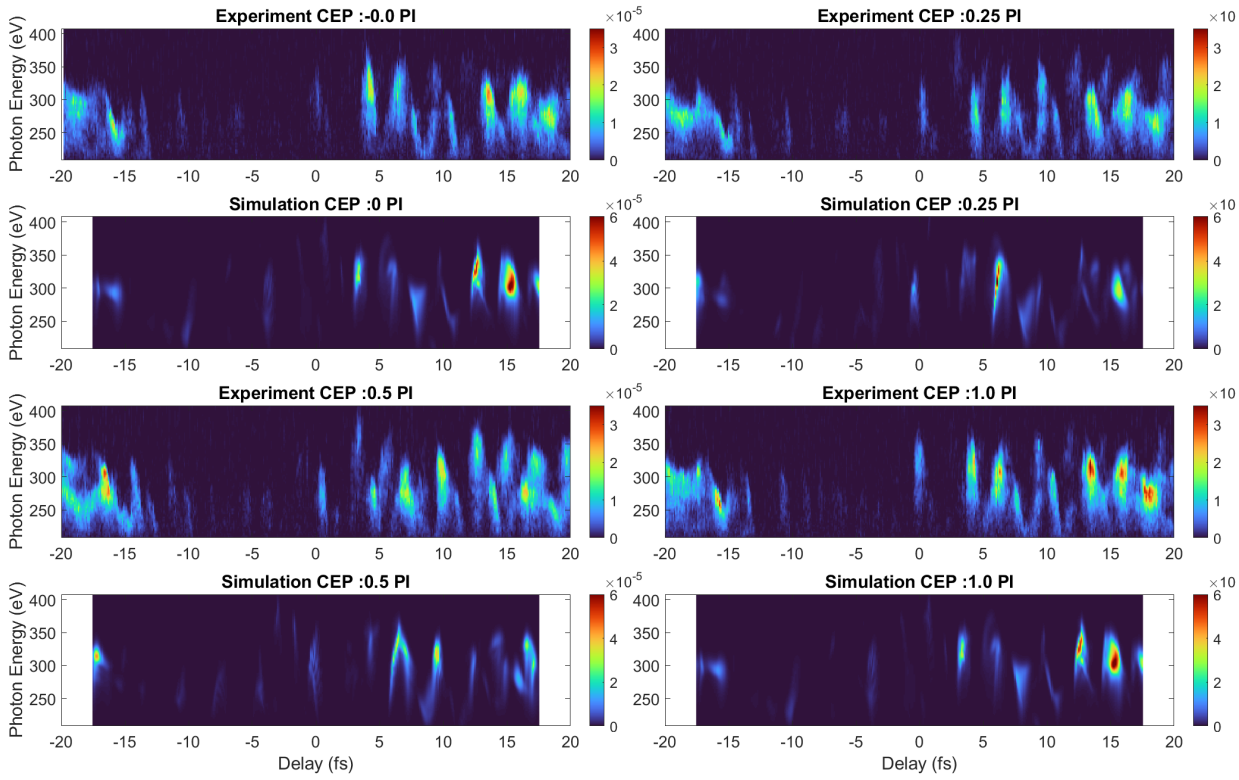

Figure 29: **Experimental and simulated delay scans in Neon** for 190 μJ synthesizer pulse energy (ND0.0).

2.11 Photon flux/efficiency calculations

This subsection considers two benchmarks that are relevant for the conclusions of this work: (I) for the IR-only photon flux calculations, the 1D optical field propagation and propagation with the Luna code resulted approximately in the same HHG yield; (II) the simulated photon flux for the case of Neon has a remarkable agreement even with the 1D code simulating the synthesised pulses. The first conclusion allows us to plot IR-only (on-axis) results from the 2D code and compare them with results obtained from the 1D code. The second conclusion is, that even when neglecting

plasma defocusing as done with the 1D code, the flux is not overestimated by orders of magnitude and can actually very well describe the experimental behaviour. The same cannot be expected from the 2D code, because a more precise knowledge of the wavefront would be necessary to accurately simulate the plasma defocusing that occurs experimentally.

To support the first benchmark, we present the data in figure 30. The HHG predictions for the same pulse energy show similar functional behaviour for the maximum flux under a certain macroscopic condition. In addition, slight differences concerning the cutoff occur for the higher pulse energies.

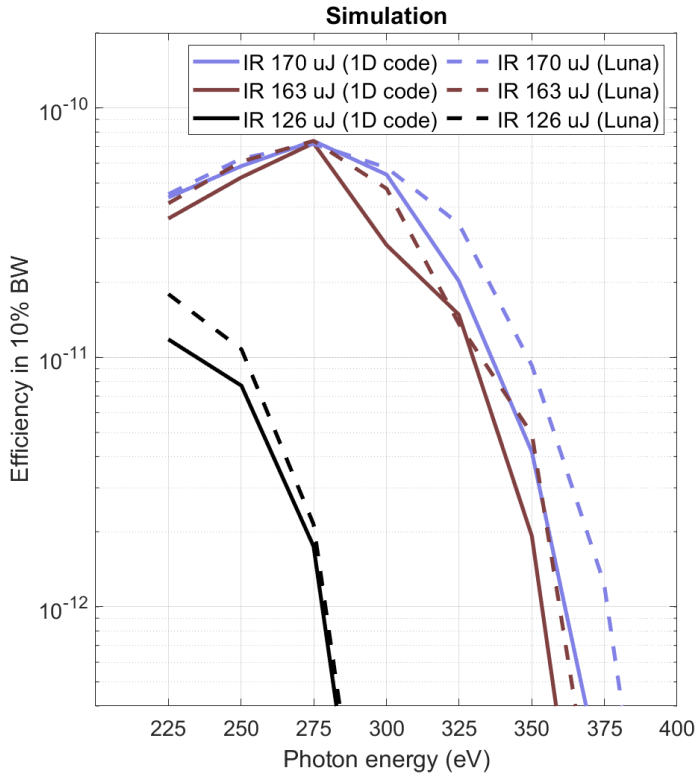

Figure 30: **1D vs. Luna Code** For the same macroscopic conditions, the optimal IR-only efficiencies at each photon energy for the 2D (Luna - dashed lines) and 1D codes (solid lines) are plotted.

Concerning the results for Neon, we present figure 31. For almost all the simulated curves, a slightly lower cutoff is achieved, which could be corrected by running a set of simulations at slightly higher intensities or averaging intensities within the experimental variations of 5%. For example, 197μJ, an energy 4% larger than the highest synthesised pulse used (190μJ), is also plotted. This pulse energy shows a better efficiency agreement in the cutoff region.

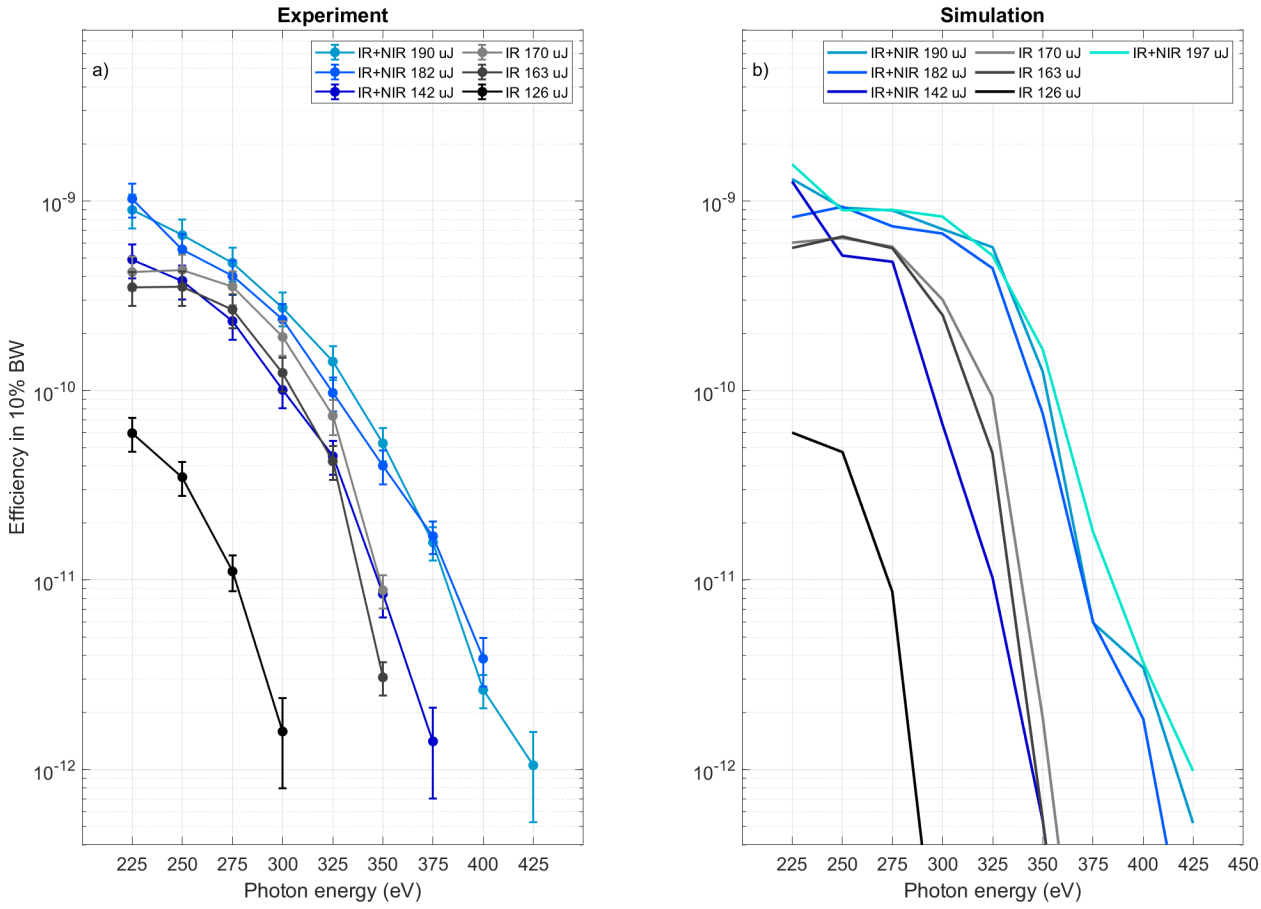

Figure 31: **Comparison of HHG efficiencies obtained in the experiment with those obtained in simulations.** In this comparison non-IAP filtered HHG and all synthesis parameters are considered when computing the efficiency. The IR-only cases made use of the 2D (Luna) code and the IR+NIR simulations were computed with our custom 1D code.

458 It is worth mentioning that the cutoff extension up to 400 - 425 eV is a kind of waveform
459 tailoring different from the ones exploited in the main manuscript. In the case of Neon the ionisa-
460 tion of the IR-only field is already close to the maximum allowed ionisation in Neon for efficient

phase matching. When this limit is severely exceeded with the synthesised fields, a depletion region appears in the HHG Delay scans (Figs. 27-29). Hence, only larger delays (see Fig.12b), that only finely tune the IR-cycle shape keeping a similar intensity to the IR-only HHG, are able to phase match efficiently. The shaping makes the recombination half-cycle longer, allowing greater acceleration and an extended cutoff relative to the IR-only HHG.

A corresponding flux analysis for Helium is shown in Fig. 32. The highest simulated efficiencies considering all synthesis parameters and also non-IAP filtered HHG are compared with the experimental data. Also the IAP flux from the main text is plotted in dashed, low opacity, lines for comparison. One notices there seems to be an overestimation of the efficiencies if the scaling factor is chosen to match the ND02 IR-only efficiency at 225 eV. If one chooses ND01 IR-only as a reference instead (Fig.32 (c)), then a better agreement is obtained. For comparison, a 4% more intense 131 μJ IR-only driver simulation is also plotted, as done for the Neon results (Fig. 31).

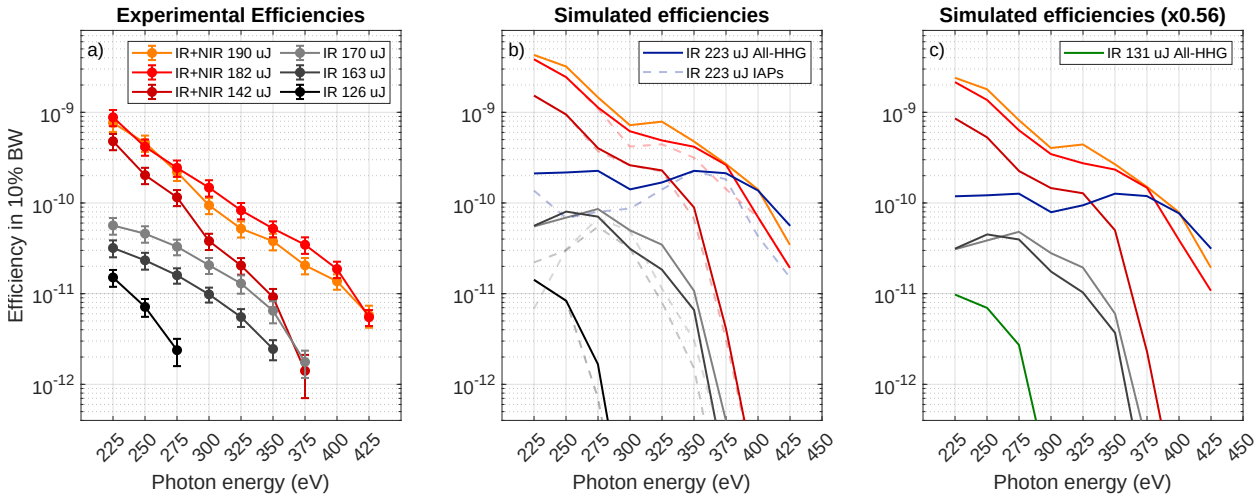

Figure 32: **Simulated efficiencies** In (a), the maximum experimental HHG efficiencies are plotted for comparison with simulations (b,c). In (b), both the maximum simulated non-IAP filtered HHG (solid lines) and IAP efficiencies (dashed) are plotted, following the same colors as in (a). In blue, the maximum IR-only energy that still allows production of IAPs is plotted. The scaling factor is chosen based on the result for the 126 μJ IR simulation. In (c), the scaling factor is changed to match the higher IR-only pulse energies and a 131 μJ IR driver simulation is also plotted.

In Fig. 33, the simulations for the macroscopic conditions of Fig. 18 (GC2, $z_R = 2$ mm) are shown. The same scaling factor as in Fig. 32(c) was used and the same order of magnitude of flux as in the latter is observed. This shows that the results are robust relative to uncertainties in the macroscopic parameters. If the RP-CEP scans are simulated with the 2D code, even though many features do not agree with the experiment, it is still possible to compare the photon flux. This comparison is done also in Fig. 33. One notices that the 2D code produces an underestimation of the enhancement achieved experimentally. This can be seen comparing the 142 μJ IR+NIR and

170 μJ IR case. One would expect the synthesised pulse to produce HHG more efficiently as in the experimental case. On the other hand, the 1D code slightly overestimates the yield.

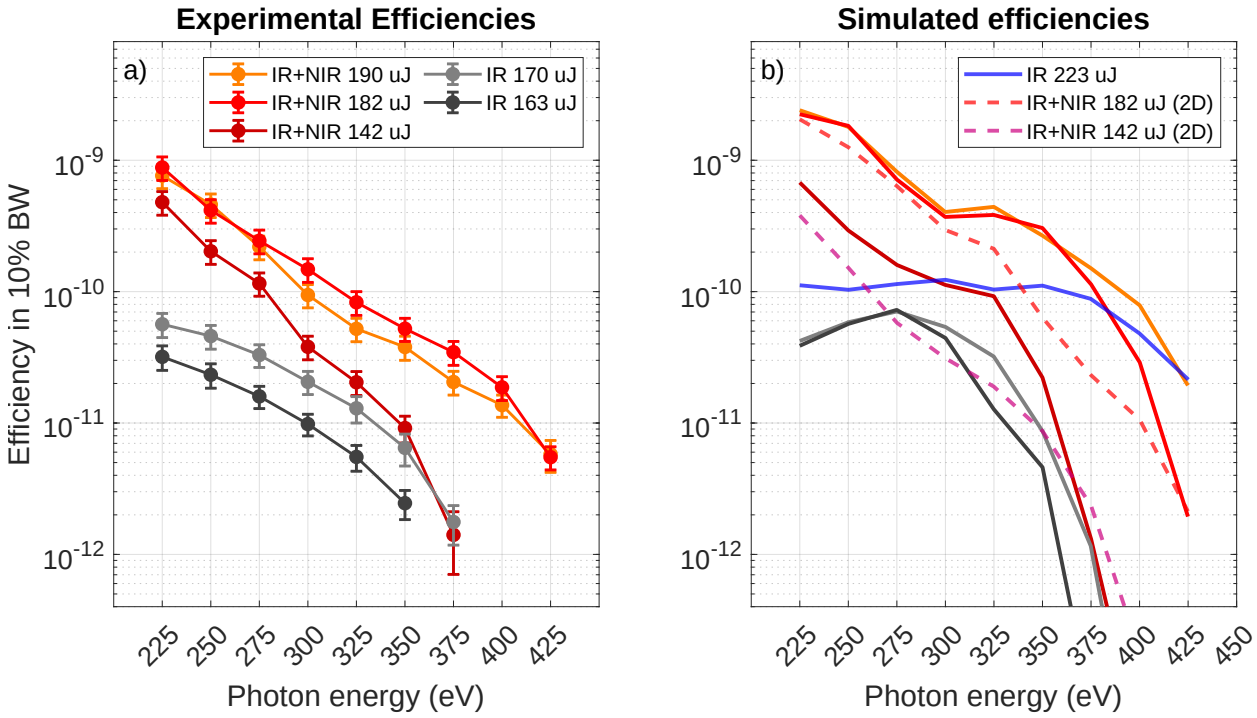

Figure 33: **Simulated efficiencies** In (a), the maximum experimental efficiencies are plotted for comparison with simulations (b). For one of the macroscopic conditions of Fig. 18 (GC2, z_R = 2 mm), a full set of simulations was done (solid lines) and the same scaling factor as in Fig. 32(c) was applied. For this same set of parameters, 2D simulations in Luna were performed also for two synthesis cases (142 μJ and 182 μ J in dashed lines). The whole HHG flux is considered in (b) without any IAP filtering.

2.12 Effect of input pulse energy on efficiency

To further support our benchmarking, the cases of flux at higher IR and IR+NIR pulse energies are simulated keeping a constant pressure and focusing position as in the experiment. Further optimization could be done by tuning these two parameters. Experimentally, however, the multi-bar pressure levels in Helium set anyway a constraint of how much it can actually be increased. For the IR-only results, the 2D code was used. For synthesised waveforms, the 1D code was used. The 223, 246 and 268 μJ energies correspond to simulation peak intensities of 500, 550 and 600 TW/cm^2 respectively. For the IR+NIR cases, an IR peak intensity of 440 TW/cm^2 and 600 TW/cm^2 was used for the 220 μJ and 296 μJ curves, respectively. The NIR intensity follows the same ratio from the 182 μJ macroscopic condition (I_{NIR} =0.37I_{IR}). For the IR-only driver, the production of IAPs stops to occur at energies above 223 μJ, and at 268 μJ the non-IAP filtered HHG efficiency also starts to drop. In the case of the synthesised drivers, because of the flexibility of tailoring the field for emission at a certain photon energy, it is possible to keep the efficiency for IAP generation even at higher pulse energies or peak intensities.

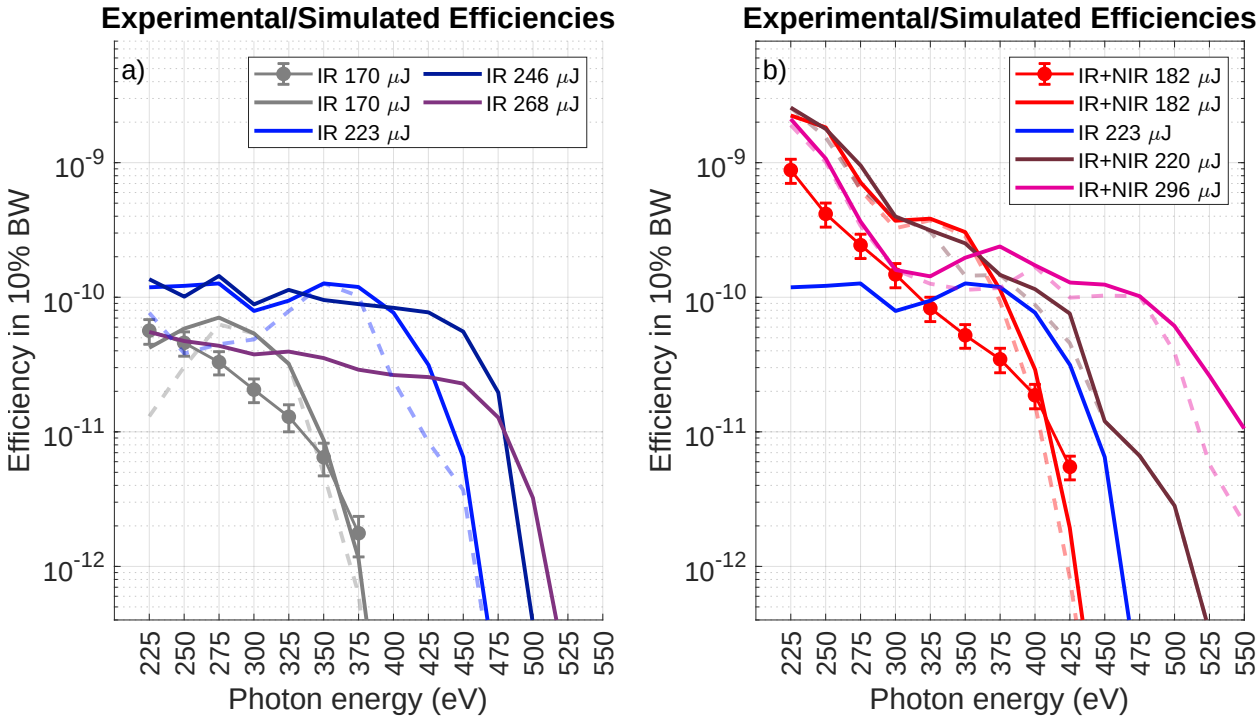

Figure 34: **Simulated efficiencies** In (a), the experimental curve for IR-only maximum efficiency at different photon energies is compared with the simulated curves for different IR pulse energies. Solid lines represent the non-IAP filtered HHG efficiency and dashed lines of the same color correspond to the IAP production efficiency. The dots with a guiding line present the measured experimental values. In (b), the same comparison is made for the synthesised pulses at different pulse energies, with one IR-only curve for comparison. The same scaling parameter as in Fig. 32(c) is used.

1. Kubullek, M. *et al.* Complete electric field characterization of ultrashort multicolor pulses. *Ultrafast Science* **5**, 0081 (2025).

2. Malitson, I. H. Interspecimen comparison of the refractive index of fused silica∗,†. *J. Opt. Soc. Am.* **55**, 1205–1209 (1965).

3. Li, J. *et al.* Polarization gating of high harmonic generation in the water window. *Applied Physics Letters* **108**, 231102 (2016).

4. Teichmann, S. M., Silva, F., Cousin, S. L., Hemmer, M. & Biegert, J. 0.5-keV Soft X-ray attosecond continua. *Nature Communications* **7**, 11493 (2016).

5. Li, J. *et al.* 53-attosecond x-ray pulses reach the carbon k-edge. *Nature Communications* **8**, 186 (2017).

6. Fraser, G. *et al.* The x-ray energy response of silicon part a. theory. *Nuclear Instruments and Methods in Physics Research Section A: Accelerators, Spectrometers, Detectors and Associated Equipment* **350**, 368–378 (1994).

7. Geissler, M. *et al.* Light propagation in field-ionizing media: Extreme nonlinear optics. *Phys. Rev. Lett.* **83**, 2930–2933 (1999).

8. Gaarde, M. B., Tate, J. L. & Schafer, K. J. Macroscopic aspects of attosecond pulse generation. *Journal of Physics B: Atomic, Molecular and Optical Physics* **41**, 132001 (2008).

9. Brabec, T. & Krausz, F. Nonlinear optical pulse propagation in the single-cycle regime. *Phys. Rev. Lett.* **78**, 3282–3285 (1997).

10. Bellini, M. *et al.* Temporal coherence of ultrashort high-order harmonic pulses. *Phys. Rev. Lett.* **81**, 297–300 (1998).

11. Brahms, C. & Travers, J. C. Luna.jl. Github (2025). URL `https://github.com/LupoLab/Luna.jl`.

12. Ammosov, M. V. & Krainov, V. P. Tunnel ionization of complex atoms and of atomic ions in an alternating electromagnetic field .

13. Tong, X. M., Zhao, Z. X. & Lin, C. D. Theory of molecular tunneling ionization. *Physical Review A* **66** (2002).

14. Tong, X. M. & Lin, C. D. Empirical formula for static field ionization rates of atoms and molecules by lasers in the barrier-suppression regime. *Journal of Physics B: Atomic, Molecular and Optical Physics* **38**, 2593–2600 (2005).

15. Perelomov, A. M., Popov, V. S. & V., T. M. Ionization of atoms in an alternating electric field. *Soviet Physics - JETP* **23**, 924 (1966).

16. Agarwal, M., Scrinzi, A. & Yakovlev, V. S. A general approximator for strong-field ionization rates (2025). URL `http://arxiv.org/abs/2507.03996`. ArXiv:2507.03996 [physics].

17. Scrinzi, A., Geissler, M. & Brabec, T. Ionization Above the Coulomb Barrier. *Physical Review Letters* **83**, 706–709 (1999).

18. Varoutis, S., Valougeorgis, D., Sazhin, O. & Sharipov, F. Rarefied gas flow through short tubes into vacuum. *Journal of Vacuum Science & Technology A* **26**, 228–238 (2008).